



## Broadband ambient noise surface wave tomography across the United States

G. D. Bensen,<sup>1</sup> M. H. Ritzwoller,<sup>1</sup> and N. M. Shapiro<sup>2</sup>

Received 26 June 2007; revised 12 September 2007; accepted 24 December 2007; published 15 May 2008.

[1] This study presents surface wave dispersion maps across the contiguous United States determined using seismic ambient noise. Two years of ambient noise data are used from March 2003 through February 2005 observed at 203 broadband seismic stations in the US, southern Canada, and northern Mexico. Cross-correlations are computed between all station-pairs to produce empirical Green functions. At most azimuths across the US, coherent Rayleigh wave signals exist in the empirical Green functions implying that ambient noise in the frequency band of this study (5–100 s period) is sufficiently isotropically distributed in azimuth to yield largely unbiased dispersion measurements. Rayleigh and Love wave group and phase velocity curves are measured together with associated uncertainties determined from the temporal variability of the measurements. A sufficient number of measurements (>2000) is obtained between 8 and 25 s period for Love waves and 8 and 70 s period for Rayleigh waves to produce tomographic dispersion maps. Both phase and group velocity maps are presented in these period bands. Resolution is estimated to be better than 100 km across much of the US from 8–40 s period for Rayleigh waves and 8–20 s period for Love waves, which is unprecedented in a study at this spatial scale. At longer and shorter periods, resolution degrades as the number of coherent signals diminishes. The dispersion maps agree well with each other and with known geological and tectonic features and, in addition, provide new information about structures in the crust and uppermost mantle beneath much of the US.

**Citation:** Bensen, G. D., M. H. Ritzwoller, and N. M. Shapiro (2008), Broadband ambient noise surface wave tomography across the United States, *J. Geophys. Res.*, 113, B05306, doi:10.1029/2007JB005248.

### 1. Introduction

[2] The purpose of this study is to produce surface wave dispersion maps across the contiguous United States using ambient noise tomography. We present Rayleigh and Love wave group and phase speed maps and assess their resolution and reliability. These maps display higher resolution and extend to shorter periods than previous surface wave maps that have been produced across the United States using traditional teleseismic surface wave tomography methods. The maps presented form the basis for an inversion to produce a higher resolution 3-D model of  $V_s$  in the crust and uppermost mantle, but this inversion is beyond the scope of the present paper.

[3] Surface wave empirical Green functions (EGFs) can be determined from cross-correlations between long time sequences of ambient noise observed at different stations. The terms noise correlation function and EGF are sometimes used interchangeably but they differ by an additive phase factor [Lin *et al.*, 2008]. Investigations of surface wave EGFs have grown rapidly in the last several years.

The feasibility of the method was first established by experimental [e.g., Weaver and Lobkis, 2001; Lobkis and Weaver, 2001; Derode *et al.*, 2003; Larose *et al.*, 2005] and theoretical [e.g., Snieder, 2004; Wapenaar, 2004] evidence. Shapiro and Campillo [2004] demonstrated that the Rayleigh wave EGFs estimated from ambient noise possess dispersion characteristics similar to earthquake derived measurements and model predictions. The dispersion characteristics of surface wave EGFs derived from ambient noise have been measured and inverted to produce dispersion tomography maps in several geographical settings, such as Southern California [Shapiro *et al.*, 2005; Sabra *et al.*, 2005], the western US [Moschetti *et al.*, 2007; Lin *et al.*, 2008], Europe [Yang *et al.*, 2007], Tibet [Yao *et al.*, 2006], New Zealand [Lin *et al.*, 2007], Korea [Cho *et al.*, 2007], Spain [Villaseñor *et al.*, 2007] and elsewhere. Most of these studies focused on Rayleigh wave group speed measurements obtained at periods below about 20 s. Campillo and Paul [2003] showed that Love wave signals can emerge from cross-correlations of seismic coda and Gerstoft *et al.* [2006] also noticed several signals on transverse-transverse cross-correlations of ambient noise. These studies did not, however, demonstrate the consistent recovery of Love wave signals from ambient noise. Although Yao *et al.* [2006] showed phase speed results, questions about the details of phase speed measurement remained. Lin *et al.* [2008] placed both phase speed and Love wave measure-

<sup>1</sup>Center for Imaging the Earth's Interior, Department of Physics, University of Colorado at Boulder, Boulder, Colorado, USA.

<sup>2</sup>Laboratoire de Sismologie, CNRS, IGP, Paris, France.

ments on a firm foundation and showed that Love waves are readily observed using ambient noise. We follow their methodology to present phase velocity and Love wave maps here in addition to group velocity and Rayleigh wave maps. We apply ambient noise tomography on a geographical scale much larger than all previous studies. The larger spatial scale also allows us to extend the results to longer periods than in previous studies.

[4] All of the results presented here are based on the data processing scheme described by *Bensen et al.* [2007]. This method is designed to minimize the negative effects that result from a number of phenomena, such as earthquakes, temporally localized incoherent noise sources, and data irregularities. It also is designed to obtain dispersion measurements to longer periods and along longer inter-station paths than in previous studies, and, thus, increases the bandwidth and the geographical size of the study region.

[5] Previous surface wave tomography across the North American continent was based on teleseismic earthquake measurements. Several of these studies involved measurements obtained exclusively across North America [e.g., *Alsina et al.*, 1996; *Godey et al.*, 2003; *van der Lee and Nolet*, 1997] whereas others involved data obtained globally [e.g., *Trampert and Woodhouse*, 1996; *Ekström et al.*, 1997; *Ritzwoller et al.*, 2002]. Ambient noise tomography possesses complementary strengths and weaknesses to traditional earthquake tomography. Single-station earthquake tomography benefits from the very high signal-to-noise ratio of teleseismic surface waves and the dispersion measurements extend to very long periods (>100 s) which results in constraints on deep upper mantle structures. Several characteristics limit the power of traditional earthquake tomography for regional to continental scale studies, however. First, teleseismic propagation paths make short period (<20 s) measurements difficult to obtain in aseismic regions due to the scattering and attenuation that occur as distant waves propagate. This is unfortunate because short period measurements are needed to resolve crustal structures. This is particularly disadvantageous across the US, which exhibits a low level of seismicity in most regions. Second, the long paths also result in broad lateral sensitivity kernels which limits resolution to hundreds of kilometers. Third, dispersion measurements from earthquakes typically have unknown uncertainties, unless measures such as cluster analysis from recurring events are employed [*Ritzwoller and Levshin*, 1998]; such cluster analysis is still limited to a subset of paths. Finally, uncertainties in source location and depth manifest themselves in uncertainties in the “initial phase” of the measurement, which imparts an ambiguity to phase and group speeds measured from earthquakes. Some of these differences can be overcome by two-station phase velocity measurements [*Tanimoto and Sheldrake*, 2002] but advantages of the ambient noise technique for regional to continental scale studies remain.

[6] Although the EGFs obtained by cross-correlating long time series between pairs of stations demonstrate a smaller signal-to-noise ratio than large earthquakes and the resulting ambient noise dispersion measurements typically are limited to periods well below 100 s, ambient noise tomography improves on each of the shortcomings of traditional earthquake tomography. First, ambient noise EGFs provide dispersion maps to periods down to  $\sim 6$  s (and lower in

some places with exceptionally dense station spacing), potentially with much better lateral resolution, particularly in the context of continental arrays of seismometers in which path density and azimuthal coverage can be very high. Second, one can estimate uncertainties from the repeatability of ambient noise measurements [e.g., *Bensen et al.*, 2007]. Third, the station locations and the “initial phase” of the EGFs are both well known [*Lin et al.*, 2008], so the measurements tend to be both more precise and more easily interpreted than earthquake signals.

[7] Ambient noise tomography, therefore, provides a significant innovation in seismic methodology that is now yielding new information about the Earth with resolutions near the inter-station spacing. The currently developing Transportable Array component of EarthScope/USArray is being deployed on a rectangular grid and is now being used across the western US for ambient noise tomography by *Moschetti et al.* [2007]. Its traverse across the United States will not complete until the year 2014, however.

[8] This paper is one of the first continental scale applications of ambient noise tomography and is based on 203 permanent and temporary broadband stations throughout the contiguous US and in southern Canada and northern Mexico (Figure 1a). Rayleigh wave tomography maps are created from 8 to 70 s period and Love wave maps from 8 to 25 s period. We present a subset of these maps. These maps provide new information about the crust and mantle beneath the United States, show that the technique is not limited to short periods or regional scales, and add further credibility to ambient noise surface wave tomography.

## 2. Data Processing

[9] We follow the method described in detail by *Bensen et al.* [2007] for data processing from observations of ambient seismic noise to the production of group speed measurements. Phase speed measurements and Love wave data processing follow the procedure of *Lin et al.* [2008]. We briefly review here the data processing procedure and discuss the repeatability of the dispersion measurements as well as the way in which signal-to-noise ratio (SNR) varies with period and region. In later sections, we discuss how measurements from almost 20,000 inter-station paths are selected to be used for tomographic inversion to estimate group and phase speed dispersion maps [*Barmin et al.*, 2001] ranging from 8 to 70 s period for Rayleigh waves and 8 to 25 s period for Love waves.

[10] We processed all available vertical and horizontal component broadband seismic data from the 203 stations (Figure 1a) that are available from the IRIS DMC and the Canadian National Seismic Network (CNSN) for the 24-month period from March 2003 through February 2005. Although the data come from this 24-month window, most time series are shorter than 24-months because of station down time or installation during this period. Time series lengths are referred to in terms of the time window from which the waveforms derived, but actual time series lengths vary within the same time window. Station locations are identified in Figure 1a. Station coverage in the west and parts of the eastern mid-west is good, but the north-central US and the near-coastal eastern US are poorly covered. As seen later, this has ramifications for

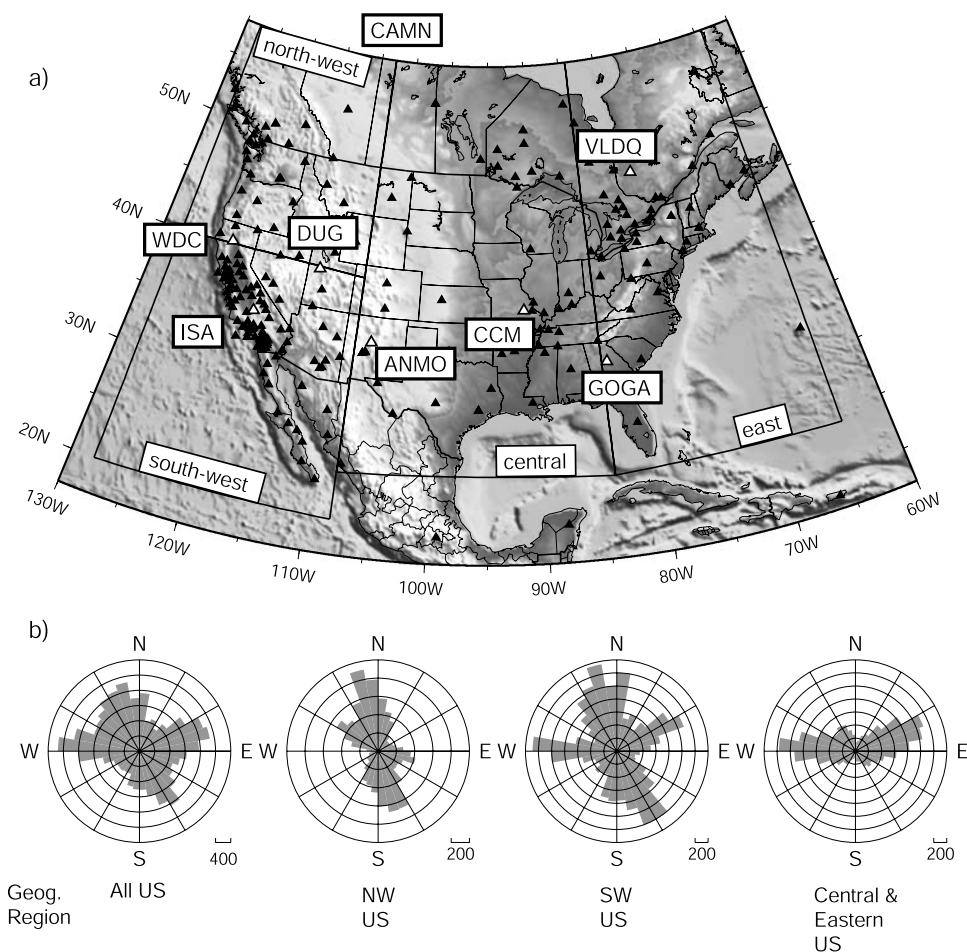


**Figure 1.** (a) The study area with stations represented as triangles. Larger white triangles with station names indicate inter-station paths for the waveforms and dispersion curves in Figure 2. The study area is divided into four boxed sub-regions. (b) Azimuthal distribution of inter-station paths, plotted as the number of paths per  $10^\circ$  azimuthal bin, for the entire data set (at left) and in several sub-regions. Both azimuth and back-azimuth are included and indicate the direction of propagation of waves. Station CAMN is just north of the map boundary at  $63.76, -110.89$ .

resolution. The azimuthal distribution of inter-station paths is shown in Figure 1b. This includes both inter-station azimuth and back-azimuth, presented as the number of paths falling into each  $10^\circ$  azimuth bin. Large numbers at a particular azimuth (or back-azimuth, both are included) correspond to the dominant inter-station directions. For example, in the eastern and central US, stations are oriented dominantly to pick up waves traveling to the north-east or the west. Concentrations of stations, such as in California, tend to produce large numbers of inter-station directions in a narrow azimuthal range. The diagrams are not azimuthally symmetric because azimuth and back-azimuth are not exactly  $180^\circ$ -complements. Figure 1b dominantly reflects the geometry of the seismic network used. Later in the paper, we discuss the directions of propagation of the strongest signals and reference them to the azimuthal distribution of inter-station paths shown in Figure 1b.

[11] Data preparation is needed prior to cross-correlation. Starting with instrument response corrected day-long time series at each station, we first perform time domain normalization to mitigate the effects of large amplitude events (e.g., earthquakes and instrument glitches). Initially, researchers

favored a 1-bit (or sign bit, or binary) normalization [Larose *et al.*, 2004; Shapiro *et al.*, 2005], but Bensen *et al.* [2007] argued for the application of a temporally variable weighting function to retain more of the small amplitude character of the raw data and to allow for flexibility in defining the amplitude normalization in particular period bands. Here, we define the temporal normalization weights between periods of 15 and 50 s, but apply the weights to the unfiltered data. As discussed by Bensen *et al.* [2007], this removes earthquakes from the daily time series more effectively than defining the temporal normalization on the raw data. The impact is seen most strongly in the quality of the Love wave signals. This procedure is applied to both the vertical and horizontal component data, but the relative amplitudes of the two horizontal components must be maintained. An additional spectral whitening is performed to all of the waveforms for each day to avoid significant spectral imbalance. Again, the same filter must be applied to both horizontal components. Spectral whitening increases the bandwidth of the automated broadband dispersion measurements [Bensen *et al.*, 2007]. After temporal and spectral normalization, cross-correlation is performed on day-long time series for vertical-vertical,

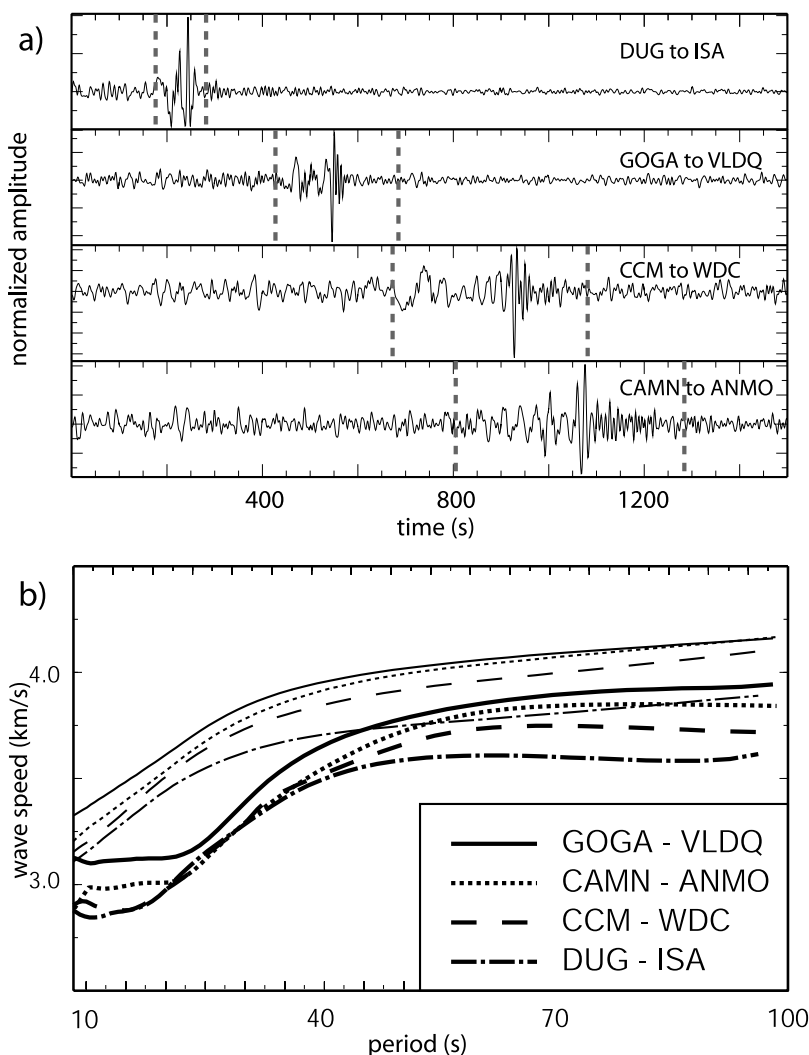


**Figure 2.** Examples of broadband vertical-component symmetric signal empirical Green functions (Rayleigh waves) through various tectonic regimes for the inter-station paths indicated with white triangles in Figure 1a. Waveforms are filtered between 7 and 100 s period. The time windows marked with vertical dashed lines are at 2.5 and 4.0 km/s. (b) The corresponding measured group and phase speed curves. Group velocity curves are thicker than phase velocity curves.

east-east, east-north, north-east, and north-north components. The horizontal components are then rotated to radial-radial (R-R) and transverse-transverse (T-T) orientations as defined by the great circle path between the two stations. These daily results are then “stacked” for the desired length of input (e.g., one month, one year, etc.). The Rayleigh wave (Z-Z and R-R) and Love wave (T-T) cross-correlograms yield two-sided (“causal” and “anticausal”) EGFs corresponding to waves propagating in opposite directions between the stations. Both the causal and acausal EGFs are equally valid and can be used as input into the dispersion measurement routine, but may have different spectral content and signal-to-noise ratio characteristics. Both for simplicity and to optimize the bandwidth of the EGFs, we average the causal and anticausal signals into a single “symmetric signal” from which all dispersion measurements are obtained.

[12] The frequency dependent group and phase velocities from the Rayleigh and Love wave EGFs are estimated using an automated dispersion measurement routine. Following

*Levshin et al.* [1972], we performed Frequency-Time Analysis (FTAN) to measure the phase and group velocity dispersion on all recovered signals. The FTAN technique applies a sequence of Gaussian filters at a discrete set of periods and measures the group arrival times on the envelope of these filtered signals. Phase velocity is also measured and further details are given by *Lin et al.* [2008]. We used the 3D model of *Shapiro and Ritzwoller* [2002] to resolve the  $2\pi$  phase ambiguity, which is successful in the vast majority of cases. The Rayleigh and Love wave signals apparent on the EGFs are less complicated than earthquake signals because the inter-station path lengths are relatively short and the absence of body waves simplifies the signal. This allowed the automation of the dispersion measurements. Selected examples of the symmetric component Rayleigh wave waveforms and the resulting group and phase speed measurements are shown in Figures 2a and 2b. The broadband dispersive nature of these waveforms is seen in Figure 2a with longer period energy arriving first. Figure 2b

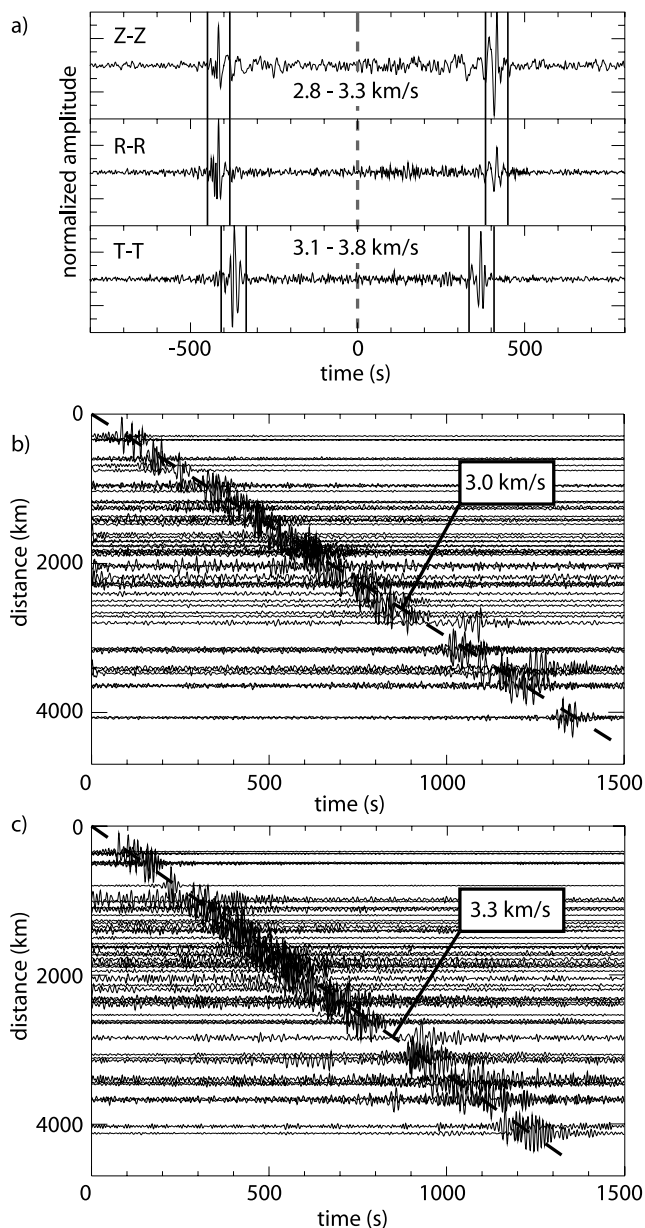


**Figure 3.** Example Rayleigh and Love wave empirical Green functions (EGFs). (a) Two-sided EGFs filtered between 5 and 50 s period for the stations CCM and RSSD. Rayleigh wave signals emerge on the Z-Z and R-R empirical Green functions (EGFs) and are highlighted with a velocity window from 2.8–3.3 km/s. Love waves are seen on the T-T component, identified with an arrival window from 3.1–3.8 km/s. (b) Record section containing all EGFs between Z-Z components from GSN stations in the US separated by the specified inter-station distance. (c) Same as Figure 3b, but for the T-T component. Move outs of 3.0 and 3.3 km/s are indicated in Figures 3b and 3c, respectively.

shows the resulting group and phase dispersion curves. The fastest path lies between stations GOGA (Godrey, GA, USA) and VLDQ (Val d’Or, Quebec, Canada) in the tectonically stable part of eastern North America. The slowest path is between stations DUG (Dugway, AR, USA) and ISA (Isabella, CA, USA) in the tectonically

active part of the western US. The other two paths (Camsell Lake, NWT, Canada to Albuquerque, NM, USA; Cathedral Cave, MO, USA to Whiskeytown Dam, CA, USA) have intermediate speeds and propagate through a combination of tectonically deformed and stable regions.

[13] Examination of the Rayleigh and Love wave signals reveals the difference between the speeds and signal strengths. Figure 3 presents examples of Z-Z, R-R, and T-T EGFs in the period range from 5 to 50 s. Figure 3a contains the EGFs between stations CCM (Crystal Cave, MO, USA) and RSSD (Black Hills, SD, USA) with an inter-station distance of 1226 km. Rayleigh waves are seen on the vertical-vertical (Z-Z) and radial-radial (R-R) cross-correlograms and arrive at similar times. Love wave signals are seen on the transverse-transverse (T-T) cross-correlograms. The different Rayleigh and Love wave arrival times are clear and are identified with different velocity windows in the diagram. Figures 3b and 3c presents record sections for the Z-Z and T-T cross-correlograms from the 13 Global Seismic Network (GSN) stations [Butler *et al.*, 2004] in the study region. Approximate move outs of 3.0 and 3.3 km/s for Rayleigh and Love waves are shown in Figures 3b and 3c, respectively.

### 3. Data Selection

[14] After the EGFs are computed between every station-pair for the Z-Z and T-T components, several selection criteria are applied prior to tomography. The effect of each step of the process in reducing the data set is indicated in Tables 1 and 2.

[15] First, we apply a minimum three wavelength inter-station distance constraint, which is imposed because of measurement instabilities at shorter distances. This criterion significantly reduces the number of measurements at periods above 50 s because stations must be separated by more than 600 km.

[16] Second, we apply a selection criterion based on the period-dependent signal-to-noise ratio (SNR), which is defined as the peak signal in a signal window divided by the root-mean square (RMS) of the trailing noise, filtered with a specified central period. Average SNR values for the Z-Z, R-R, and T-T EGFs are seen in Figure 4a. A dispersion measurement is retained at a period if the SNR > 15 for the EGF at that period. A lower SNR value is accepted if the measurement variability is small, as will be described below.

**Table 1.** Number of Rayleigh Wave Measurements Rejected and Selected Prior to Tomography at 10-, 16-, 25-, 50-, and 70-s Periods

<i>Period</i>	10-s	16-s	25-s	50-s	70-s
Total waveforms	18,554	18,554	18,554	18,554	18,554
Distance rejections	487	933	1,608	3,465	4,818
SNR < 10	7,416	5,049	5,327	9,990	10,686
<i>Group velocity rejections</i>					
Stdev > 100 m/s or undefined	3,348	3,418	3,624	2,782	1,799
3 $\sigma$ time residual rejection	182	222	104	32	29
Remaining group measurements	7,121	8,932	7,891	2,285	1,222
<i>Phase velocity rejections</i>					
Stdev > 100 m/s or undefined	3,296	3,561	3,603	1,626	941
3 $\sigma$ time residual rejection	161	321	135	58	36
Remaining phase measurements	7,194	8,690	7,881	3,415	2,073

**Table 2.** Same as Table 1 but for Love Waves

Period	10-s	16-s	25-s
Total waveforms	18,554	18,554	18,554
Distance rejections	487	933	1,608
SNR < 10	8,690	7,042	13,591
<i>Group velocity rejections</i>			
Stdev > 100 m/s or undefined	2,709	2,563	1,324
3 $\sigma$ time residual rejection	222	245	63
Remaining group measurements	6,446	7,771	1,968
<i>Phase velocity rejections</i>			
Stdev > 100 m/s or undefined	2,848	4,332	1,266
3 $\sigma$ time residual rejection	200	166	94
Remaining phase measurements	6,329	6,081	1,995

[17] Similarities in the patterns of SNR as a function of period for Rayleigh waves on the Z-Z and R-R components are observed in Figure 4a up to 20 s period; although the R-R signal quality is lower. Above 20 s period, the R-R SNR degrades more quickly, however, similar to the trend of the SNR for the T-T cross-correlations. This pattern is consistent with the results of *Lin et al.* [2008]. Apparently, the SNR degrades at longer periods on horizontal components predominantly due to increasing levels of incoherent local noise, and may not be due to decreasing signal levels. Because the SNR is much higher on the Z-Z than the R-R components and the Z-Z bandwidth is larger, we only use Rayleigh wave dispersion measurements obtained on the Z-Z EGFs.

[18] Figures 4b and 4c presents information about the geographical distribution of SNR. The average SNR of all waveforms is shown for Rayleigh (Z-Z) and Love (T-T) wave signals in each of the four regions defined in Figure 1a where both stations lie within the sub-region. SNR in the sub-regions is higher than over the entire data set (Figure 4a) because path lengths are shorter, on average, by more than a factor of two in the regional data. Rayleigh wave SNR is highest in the south-west region, with SNR in the other regions being lower but similar to each other. Long period SNR, in particular, is considerably higher in the south-west than in other regions. In most regions, the Rayleigh wave curves show double peaks apparently related to the primary and secondary microseism periods of 15 and 7.5 s, respectively.

[19] For Love waves, the highest SNR is in the south-west and north-west regions and the curves display only a single peak near the primary microseismic band, peaking in different regions between 13 and 16 s period. The highest Love wave SNR is in the north-west, unlike the Rayleigh waves which are highest in the south-west region. This implies that the distribution of Rayleigh and Love wave energies differ and they may not be co-generated everywhere. Although Figure 4a shows that below 15 s period Love waves have a higher average SNR than Rayleigh waves, this is true only in the western US. In the central and eastern US, Rayleigh and Love waves below about 15 s have similar SNR values implying similar energy strengths. In all regions, Love wave signals are negligible above about 25 s period. Love wave signals are much stronger in the western US than in the central or eastern US, particularly above about 15 s period. These results indicate clearly that the strongest ambient noise sources are located generally in

the western US, although substantial Rayleigh wave signal levels also exist in the central and eastern US. Love waves in the central and eastern US, however, are much weaker above about 15 s.

[20] Third, we apply a data selection criterion based on the variability of measurements repeated on temporally segregated subsets of the data. We compiled EGFs for

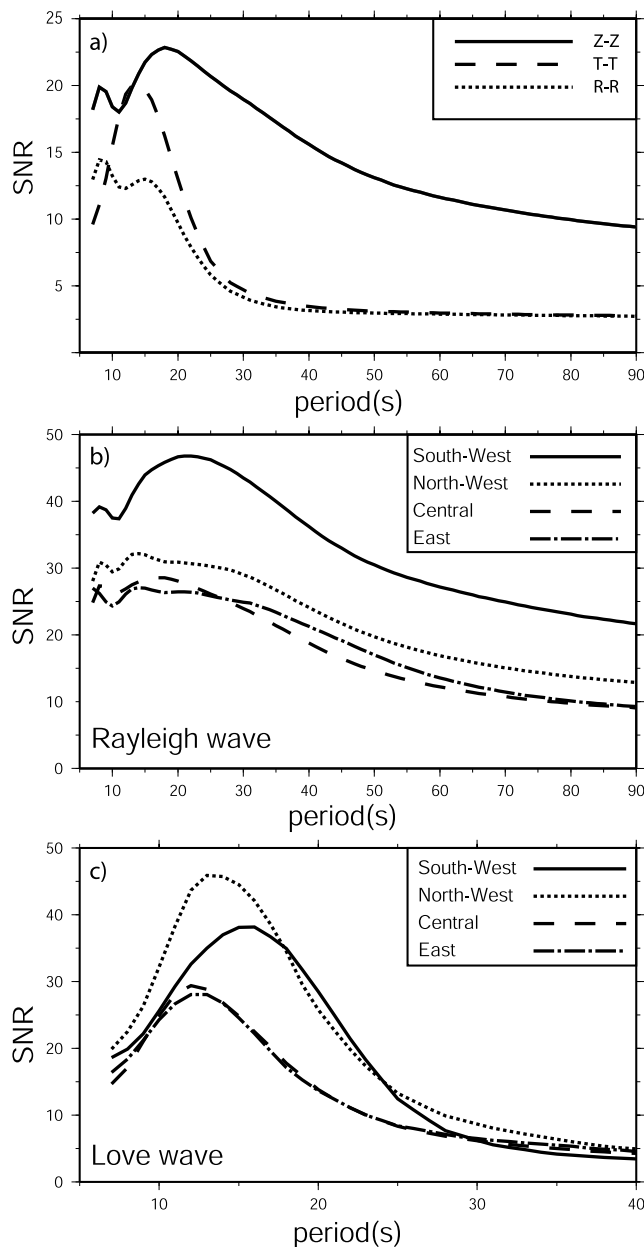


**Figure 4.** (a) Relative signal quality represented as the average signal-to-noise ratio (SNR) for Rayleigh and Love waves computed using all stations in the study region. Rayleigh waves appear on vertical-vertical (Z-Z) and radial-radial (R-R) components, while Love waves are on the transverse-transverse (T-T) component EGFs. The mean signal-to-noise ratio is plotted versus period for (b) Rayleigh (Z-Z) waves and (c) Love (T-T) waves for the different geographical sub-regions defined in Figure 1a. Note: the period bands for Figures 4b and 4c differ.

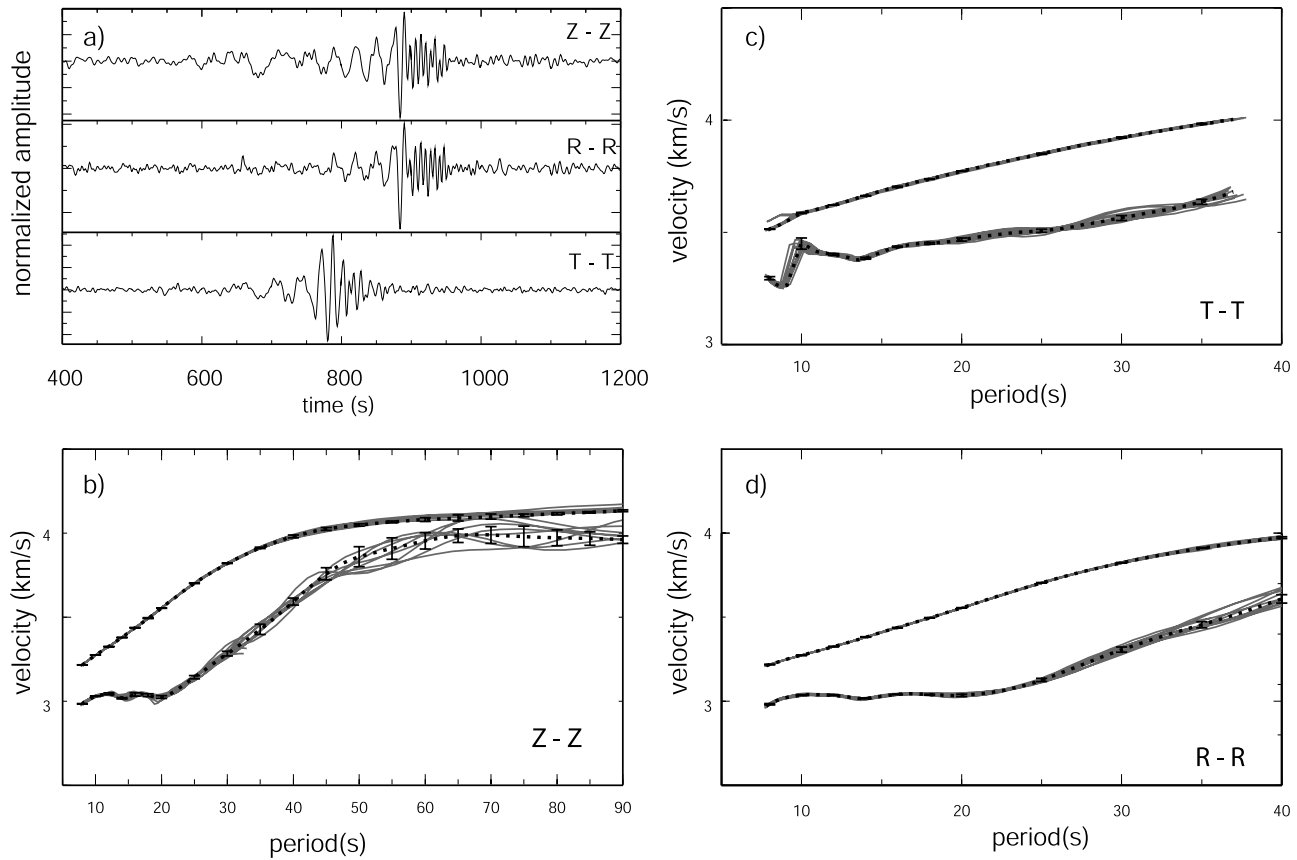


**Figure 5.** Illustration of the computation of measurement uncertainty. (a) Empirical Green functions (EGFs) on the Z-Z, R-R, and T-T components for the station pair DWPF and RSSD. (b) Measured Rayleigh wave group and phase speed curves from the Z-Z component EGF. The 24-month measurements are plotted as black dotted lines, individual 6-month measurements are plotted in grey, and the 1-σ error bars summarize the variation among the 6-month results. (c) Same as Figure 5b, but for the T-T component (Love waves). (d) Same as Figure 5b, but for the R-R component. Note the different period bands and velocity scales in Figures 5b–5d.

overlapping 6-month input time series (e.g., June, July, August 2003 plus June, July, August 2004) to obtain 12 “seasonal” stacks. We measure the dispersion curves on data from each 6-month (dual 3-month) time window and on the complete 24-month time window. For each station-pair, the standard deviation of the dispersion measurements is computed at a particular period using data from all of the 6-month time windows in which SNR >10 at that period. An illustration of this procedure appears in Figure 5. Figure 5a shows the Z-Z, R-R, and T-T EGFs used from the 2685 km long path between stations DWPF (Disney Wilderness Preserve, FL, USA) and RSSD (Black Hills, SD, USA). Figures 5b, 5c and 5d compares the measurements obtained on the 6-month temporal subsets of data with the 24-month group and phase velocity measurements. The error bars indicate the computed standard deviations. If fewer than four 6-month time series satisfy the criterion that SNR >10, then the standard deviation of the measurement is considered indeterminate and we assign three times the average of the standard deviations taken over all measurements within the data set. The average standard deviation values are shown in Figure 6. Finally, we reject measurements for a particular wave type (Rayleigh/Love, group/phase speed)

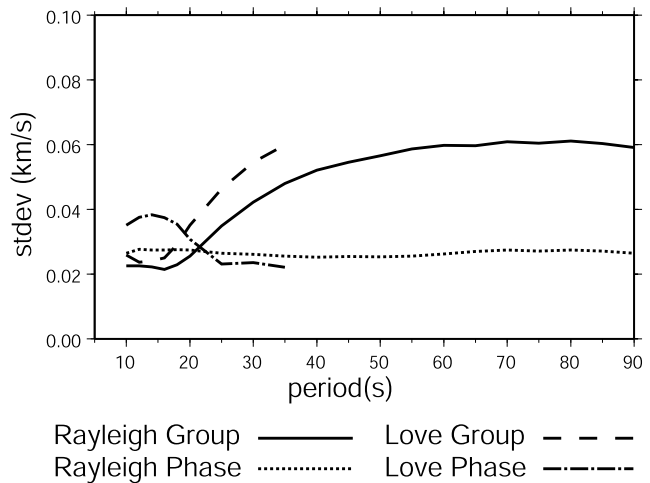


**Figure 6.** Average dispersion measurement standard deviation versus period for Rayleigh and Love wave group and phase speeds, where the average is taken over all acceptable measurements.

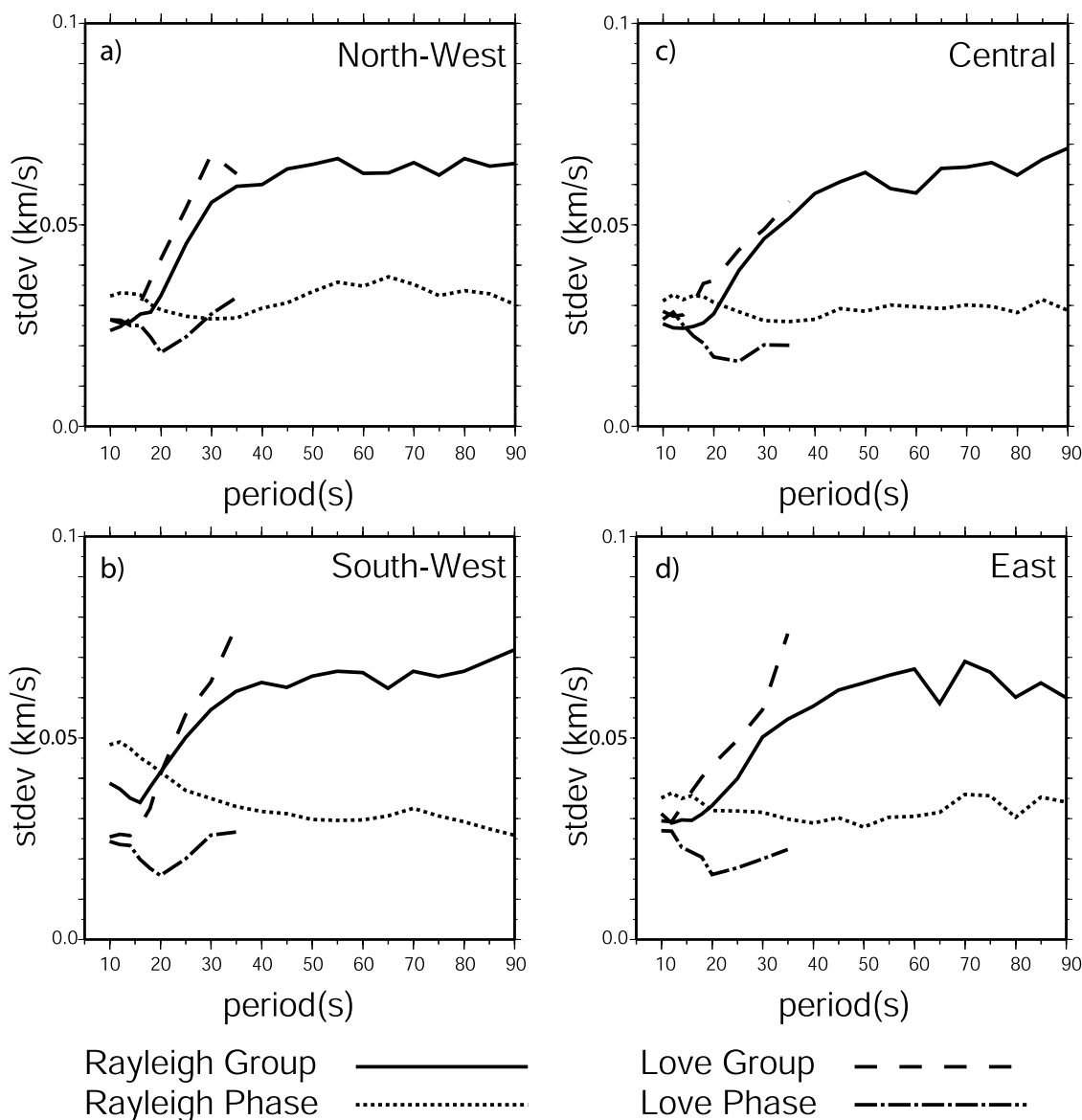


**Figure 7.** The average standard deviation of the velocity measurements as determined from the 6-month subsets of the data, averaged over all acceptable measurements. (a) - (d) Results are for the four sub-regions defined in Figure 1a.

and period if the estimated standard deviation is greater than 100 m/s, as this indicates an instability in the measurement. The inverse of the standard deviation is used as a weight in the tomographic inversion [e.g., *Barmin et al.*, 2001].

[21] In contrast with Figure 6, Figure 7 contains the mean measurement standard deviation values for each of the four sub-regions defined in Figure 1a. The measurements are labeled for Rayleigh and Love wave group and phase measurements. The patterns are similar for all sub-regions. Because dramatic differences between measurement uncertainties in different regions are not observed, similar measurement quality is obtained in all regions even though there are differences between the regions in average SNR and, therefore, different numbers of measurements in each region. The most stable measurements are Rayleigh wave phase speeds, particularly above about 20 s period where phase

speed is more robust than group speed. Below 20 s period, the envelope on which group velocity is measured becomes narrower at short periods and increases measurement precision. Thus the accuracy of the group velocity measurements becomes similar to the phase velocity measurements below 20 s period. Although the Love wave phase velocity measurements have favorable standard deviation with increasing period, the number of high quality measurements above 20 s period drops precipitously due to low signal levels. Finally, as a rule-of-thumb, at periods above about 30 s, the standard deviation of Rayleigh wave phase speed measurements is about half that of group speed.

[22] Fourth, we apply a final data selection criterion based on tomographic residuals. Using the thus far accepted measurements, we create an overly smoothed tomographic dispersion map for each wave type (Rayleigh/Love, group/

phase velocity). Measurements for each wave type with high traveltimes residuals (three times the root-mean squared residual value at a given period and wave type) are removed and the overly smoothed dispersion map is recreated, becoming the background dispersion map for a later less damped inversion.

[23] The final Rayleigh wave (Z-Z) path retention statistics for selected periods are shown in Table 1. Similar statistics for Love waves (T-T) at periods of 10, 16, and 25 s period are shown in Table 2. The number of paths retained at periods above about 70 s for Rayleigh waves and 25 s for Love waves is insufficient for tomography across the US, but the longer period measurements would be useful in combination with teleseismic dispersion measurements.

#### 4. Azimuthal Distribution of Signals

[24] The theoretical basis for surface wave dispersion measurements obtained on from EGFs and the subsequent tomography assumes that ambient noise is distributed homogeneously with azimuth [e.g., *Snieder*, 2004]. Asymmetric two-sided EGFs, such as those shown in Figure 3a and documented copiously elsewhere [e.g., *Stehly et al.*, 2006], illustrate that the strength and frequency content of ambient noise vary appreciably with azimuth. This motivates the question as to whether ambient noise is well enough distributed in azimuth to return unbiased dispersion measurements for use in tomography. *Lin et al.* [2008] present evidence, based on measurements of the “initial phase” of phase speed measurements from a three-station method, that in the frequency band they consider (6–40 s period) ambient noise is distributed sufficiently isotropically so that phase velocity measurements are returned largely unbiased. *Yang and Ritzwoller* [2008] performed synthetic experiments to quantify the effect of strongly anisotropic background noise source distribution. They found that in the presence of low level homogeneously distributed ambient noise, much stronger ambient noise in an off-axis direction affects measured phase velocities by less than 0.5%.

[25] *Stehly et al.* [2006] left the precision of group velocity measurements in doubt after showing strong azimuthal imbalance of signal strength in the western US. The reliability of group velocity measurements on such EGFs was tested by *Stehly et al.* [2007] on both the causal and anti-causal parts of EGFs. They compared measured velocity from EGFs computed from one-month duration ambient noise time series to measurements from a baseline Green function and found that measurement variability was less than 0.3% and in certain cases less than 0.02%. Even with a noise distribution shown to be decidedly inhomogeneous, there is little effect on the precision of measured group velocity.

[26] According to *Yang and Ritzwoller* [2008], therefore, to show that the measurements on EGFs used for tomography are indeed accurate, we need only show that strong signals exist in some azimuths. In this assessment, the distribution of paths dictated by the geometry of the array must be borne in mind. Consequently, all results are taken relative to the azimuthal distribution of the observing network presented in Figure 1b. In addition to solidifying confidence in EGF dispersion measurements, much can be learned about the character of the ambient noise environment in North America.

[27] Figure 8 presents the azimuthal distribution of high SNR Rayleigh wave signals at periods of 8, 14, 25, and 40 s. Our measurements are divided into three sub-regions as defined in Figure 1a, but with the central and eastern regions combined. Only one station in each station-pair is required to be in a sub-region. Both azimuth and back-azimuth are included in the figure. Averaging over all regions and azimuths, at periods of 8, 14, 25, and 40 s the fraction of Rayleigh wave EGFs with a SNR >10 is 0.38, 0.49, 0.54, and 0.38, respectively, and reduces quickly for periods above 40 s. To compute this fraction as a function of azimuth, the number of paths with SNR >10 in a given 20° azimuth bin is divided by the total number of paths in that bin given by Figure 1b. The SNR on both EGF lags is considered separately, and the indicated azimuth is the direction of propagation. We refer to the positive and negative lag contributions as having come from different “paths” for simplicity, but, in fact, the paths are the same and only the azimuths differ.

[28] Inspection of Figure 8 reveals that the fraction of relatively high SNR paths at a given azimuth is often more homogeneously distributed than the western US results of *Stehly et al.* [2007] or the synthetic results of *Yang and Ritzwoller* [2008]. At 14 and 25 s period, in all three regions all azimuths have the fraction of paths with SNR >10 above 20% and, hence, the distribution of useful ambient noise signals sufficient to imply accuracy, even though the highest SNR signals may arrive from only a few principal directions. At 8 s period, the results are not as geographically consistent. In the two western regions, the strongest signals are those with noise coming from the west. This agrees with the notion that these results would be dominated by the 7.5 s period secondary microseism. In the east and central regions, however, signals come both from the west and northeast and there are fewer high SNR EGFs. Finally, moving to 40 s period, the overall fraction of high SNR measurements is lower. Relative to this lower level, there are still azimuths where the SNR is higher, perhaps implying dominant noise source directions. The azimuthal pattern above 40 s in each region remains about the same as at 40 s, but the fraction of high SNR observations diminishes rapidly.

[29] Similar results are obtained for Love waves, as can be seen in Figure 9. Strong Love wave signals are most isotropic in the primary microseismic band, the center column in Figure 9. In the secondary microseismic band, strong Love waves are less isotropic, particularly in the Central US. Nevertheless, azimuthal coverage sufficiently homogeneous for accurate measurements. Above 20 s period, however, the number of large amplitude signals diminishes rapidly, particularly in the east. In the west, some large amplitude signals exist, but emerge dominantly from the northwest and southeast directions. Signal amplitude above 20 s period is insufficient for tomography on a large scale.

[30] A possible concern with interpreting these plots is the potential for bias by signals from short inter-station paths. In Figure 10 we show an example of the distance and azimuth distribution of signals with SNR >10 in the central-east region at 25 s period. Long distance high SNR arrivals are seen, and the distribution is mainly controlled by the array configuration. Such array induced limitations are observed in the other regions as well.

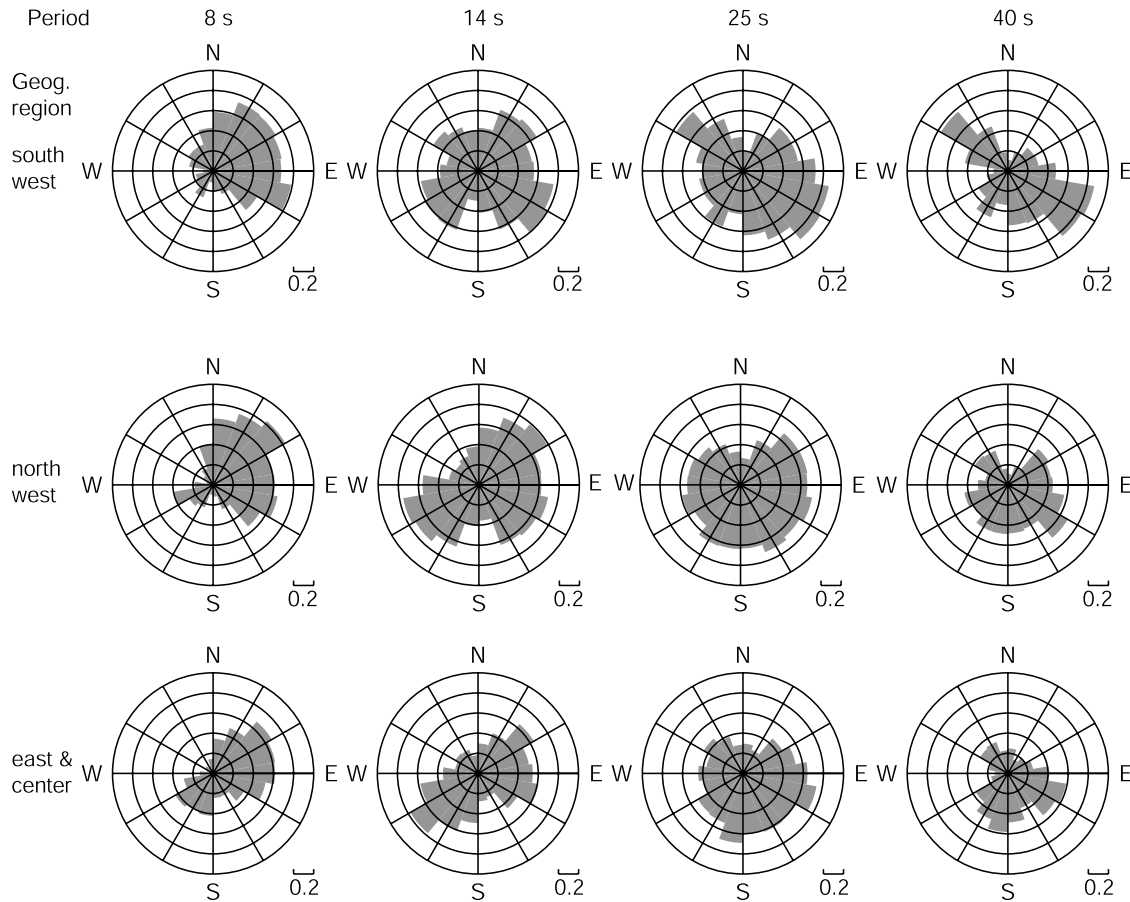


**Figure 8.** The directional dependence of high SNR (>10) Rayleigh wave EGF signals plotted at different periods (8, 14, 25, 40 s in different columns) and geographical sub-regions (different rows). Azimuth is the direction of propagation of the wave. Results are presented as fractions, in which the numerator is the number of inter-station paths in a particular azimuthal bin with SNR > 10 and the denominator is the number of paths in the bin (from Figure 1b).

[31] In conclusion, therefore, at all periods studied, in all regions and most azimuths, a useful level of coherent Rayleigh wave signals exist in ambient noise. Stronger azimuthal imbalance is most pronounced at periods below 10 s, where most of the Rayleigh wave energy is coming generally from the west. Coherent Love wave signals exist at most azimuths from 8 s to 20 s period, but at longer periods both the azimuthal coverage and the strength of Love waves diminish rapidly. These observations, combined with recent theoretical and experimental work, provide another item in a growing list of evidence indicating that ambient noise in this frequency band is distributed in azimuth in such a way to yield largely unbiased dispersion measurements.

## 5. Tomography

[32] An extensive discussion of the tomography procedure was presented by *Barmin et al.* [2001]. We follow their discussion to provide a basic introduction to the overall procedure and define some needed terms. The tomographic inversion is a 2-D ray theoretical method, similar to a Gaussian beam technique and assumes wave propagation along a great circle but with “fat” rays. Starting with observed traveltimes we estimate a model  $\mathbf{m}$  (2-D distribu-

tion of surface wave slowness) by minimizing the penalty functional:

$$(\mathbf{G}(\mathbf{m}) - \mathbf{d})^T \mathbf{C}^{-1} (\mathbf{G}(\mathbf{m}) - \mathbf{d}) + \alpha^2 \|\mathbf{F}(\mathbf{m})\|^2 + \beta^2 \|\mathbf{H}(\mathbf{m})\|^2, \quad (1)$$

where  $\mathbf{G}$  is the forward operator computing traveltimes from a model,  $\mathbf{d}$  is the data vector of measured surface wave traveltimes, and  $\mathbf{C}$  is the data covariance matrix assumed here to be diagonal and composed of the square of the measurement standard deviations.  $\mathbf{F}(\mathbf{m})$  is the spatial smoothing function where

$$\mathbf{F}(\mathbf{m}) = \mathbf{m}(\mathbf{r}) - \int_S S(\mathbf{r}, \mathbf{r}') \mathbf{m}(\mathbf{r}') d\mathbf{r}', \quad (2)$$

and

$$S(\mathbf{r}, \mathbf{r}') = K_0 \exp\left(-\frac{|\mathbf{r} - \mathbf{r}'|^2}{2\sigma^2}\right) \quad (3)$$

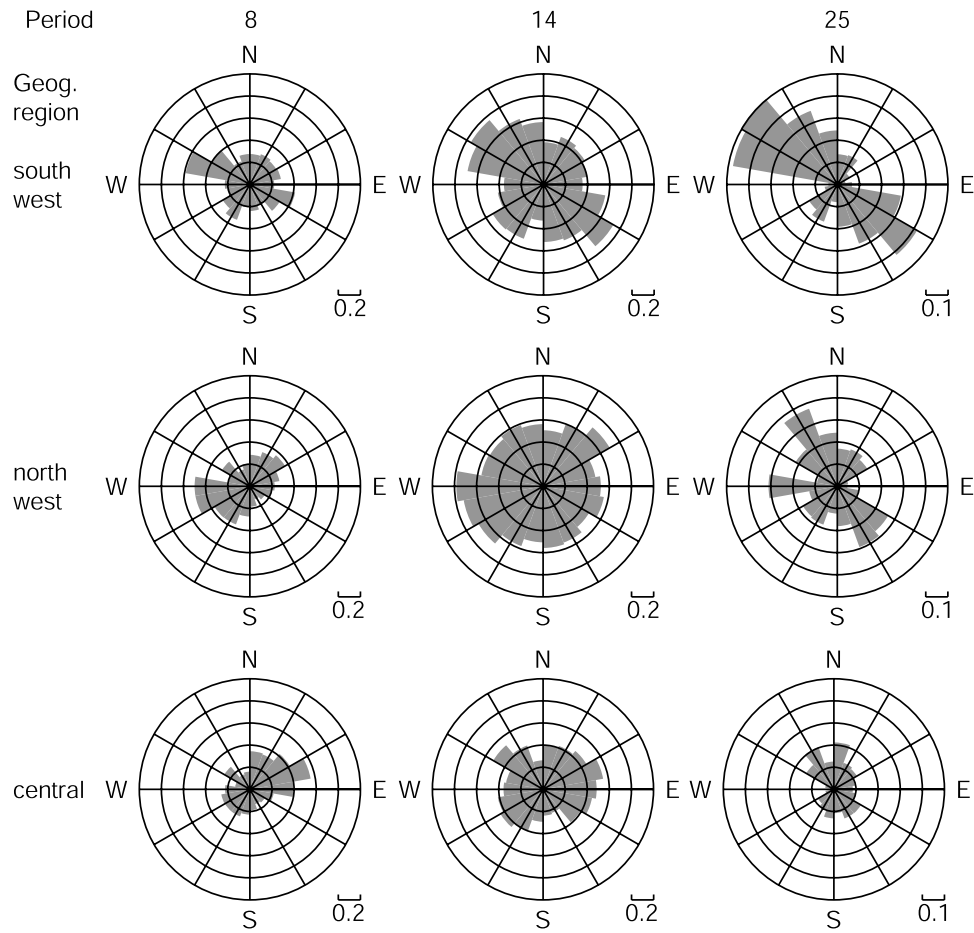


Figure 9. Same as Figure 8, but for Love waves.

where

$$\int_S S(\mathbf{r}, \mathbf{r}') d\mathbf{r}' = 1, \tag{4}$$

and  $\mathbf{r}$  is the target location and  $\mathbf{r}'$  is an arbitrary location. The functional  $H$  penalizes the model based on path density and azimuthal distribution.

[33] The contributions of  $H$  and  $F$  are controlled by the damping parameters  $\alpha$  and  $\beta$  in equation (1) while spatial smoothing (related to the fatness of the rays) is controlled by adjusting  $\sigma$  in equation (3). These three parameters ( $\alpha$ ,  $\beta$  and  $\sigma$ ) are user controlled variables that are determined through trial and error optimization.

[34] The resulting spatial resolution is found at each point by fitting a 2-D Gaussian function to the resolution matrix (map) defined as follows:

$$A \exp\left(-\frac{|\mathbf{r}|^2}{2\gamma^2}\right) \tag{5}$$

where  $\mathbf{r}$  here denotes the distance from the target point. The fit parameter is the standard deviation of the Gaussian function,  $\gamma$ , which quantifies the spatial size of the features that can be determined reliably in the tomographic maps. In

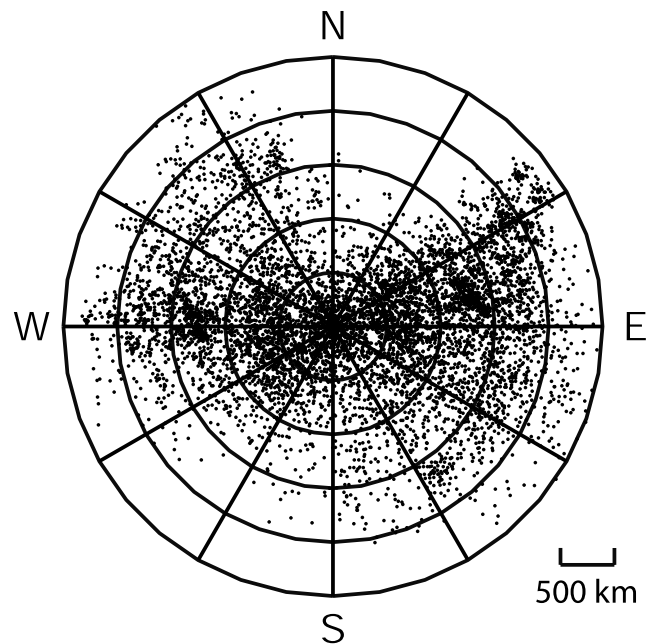
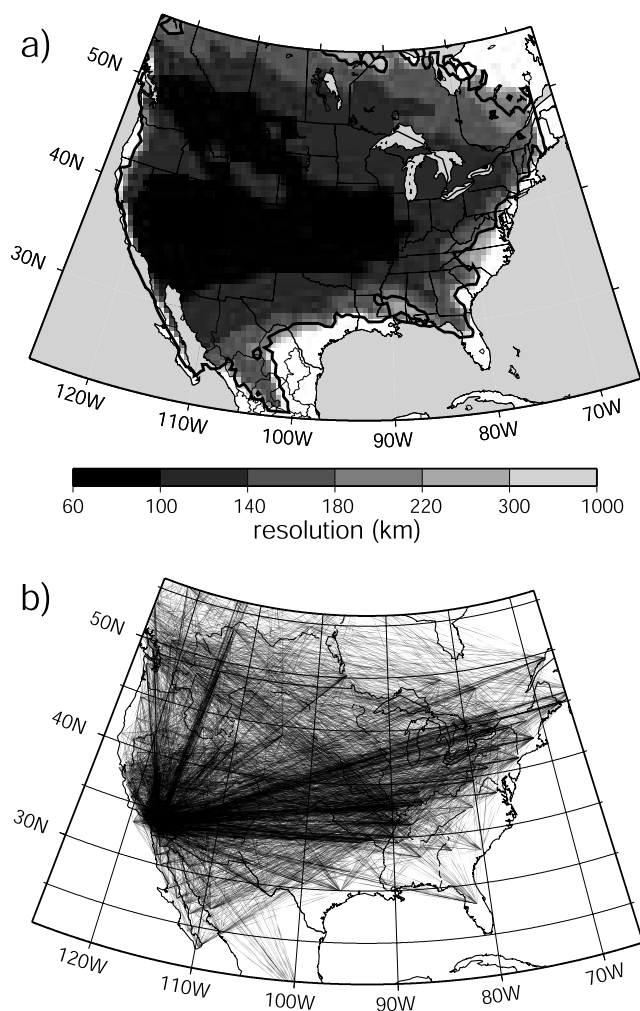


Figure 10. A plot of the azimuth and distance for all signals in the central-east region with SNR > 10 at 25 s period. The sparse regions in the N-NE and S-SW are due to the array configuration.



**Figure 11.** Path distribution and estimated resolution for the 10 s period Rayleigh wave. (a) Resolution is defined as twice the standard deviation ( $2\gamma$ ) of the 2-D Gaussian fit to the resolution surface at each point. The 200 km resolution contour is drawn and the color scale saturates at white when the resolution degrades to 1000 km, indicating indeterminate velocities. (b) Paths used to construct Figure 11a.

this paper, we report  $2\gamma$  as the resolution, the full-width of the resolution kernel at each point. Figure 11a shows the resolution map for the 10 s Rayleigh wave group speed. The corresponding ray coverage is shown in Figure 11b. The more densely instrumented regions, such as southern California and near the New Madrid seismic zone in the central United States, have resolution  $<100$  km, which is better than the inter-station spacing in these regions. Across most of the US, resolution averages about 100 km for Rayleigh waves up to 40 s period and then degrades to 200 km at 70 s period. For Love waves, resolution averages about 130 km below 20 s period, but then rapidly degrades at longer periods so that at 20 s the average resolution is about 200 km. The rapid degradation of average resolution in the US for Love waves is due to the loss of Love wave signals in the eastern US, which sets on at about 15 s period, as discussed above. Regions with resolution worse than 1000 km are indicated on the tomographic maps in grey

and, in addition, to outline the high resolution regions we plot the 200 km resolution contours.

[35] We use ray theory as the basis for tomography in this study, albeit with “fat rays” given by the correlation length parameter  $\sigma$ . In recent years, surface wave studies have increasingly moved toward diffraction tomography using spatially extended finite-frequency sensitivity kernels based on the Born/Rytov approximation [e.g., Spetzler *et al.*, 2002; Ritzwoller *et al.*, 2002; Yoshizawa and Kennett, 2002]. Ritzwoller *et al.* [2002] showed that ray theory with fat rays produces similar structure to diffraction tomography in continental regions at periods below 50 s and the similarities strengthen as path lengths decrease. Yoshizawa and Kennett [2002] argued that the spatial extent of sensitivity kernels is effectively much less than given by the Born/Rytov theory, being confined to a relatively narrow “zone of influence” near the classical ray. They conclude, therefore, that in many applications, off-great circle propagation may provide a more important deviation from straight-ray theory than finite frequency effects. Ritzwoller and Levshin [1998] show that off-great circle propagation can be largely ignored at periods above about 30 s for paths with distances less than 5000 km, except in extreme cases. From a practical perspective then, these arguments support the contention that ray-theory with ad-hoc fat rays can adequately represent wave propagation for most of the path lengths and most of the period range under consideration here. A caveat is for relatively long paths ( $>1000$  km) at short periods ( $<20$  s), in which case off-great circle effects may become important. Off-great circle effects will be largest near structural gradients, but are mitigated by observations made on orthogonal paths. In our study region, where structural gradients are largest, azimuthal path coverage tends to be quite good. These considerations lead us to conclude that ray theory with fat-rays is sufficient to produce meaningful dispersion maps and that uncertainties in the maps produced by the arbitrariness of the choice of the damping parameters are probably larger than errors induced by the simplified theory. Nevertheless, future work is needed to test this assertion quantitatively. We anticipate only subtle changes to the dispersion maps.

## 6. Results

[36] In this section we present examples of the tomographic maps with the particular purpose of establishing their credibility and limitations. In the next section, we qualitatively discuss some of the structural features that appear in the maps.

[37] The tomography method, described in the preceding section, is applied to the final set of accepted measurements to produce dispersion maps from 8 to 70 s period for Rayleigh waves and 8 to 25 s period for Love waves. In this period range more than 2000 measurements exist for all wave types. The method is applied on a  $0.5^\circ \times 0.5^\circ$  geographical grid across the study region. Examples of the resulting dispersion maps are presented in Figures 12–15. In all maps, the 200 km resolution contour is shown with a thick black or grey contour and the grey regions are those areas on the continent that have indeterminate velocities. The damping parameters  $\alpha$  and  $\beta$  in equation (1) which control the strength of the smoothness constraint and

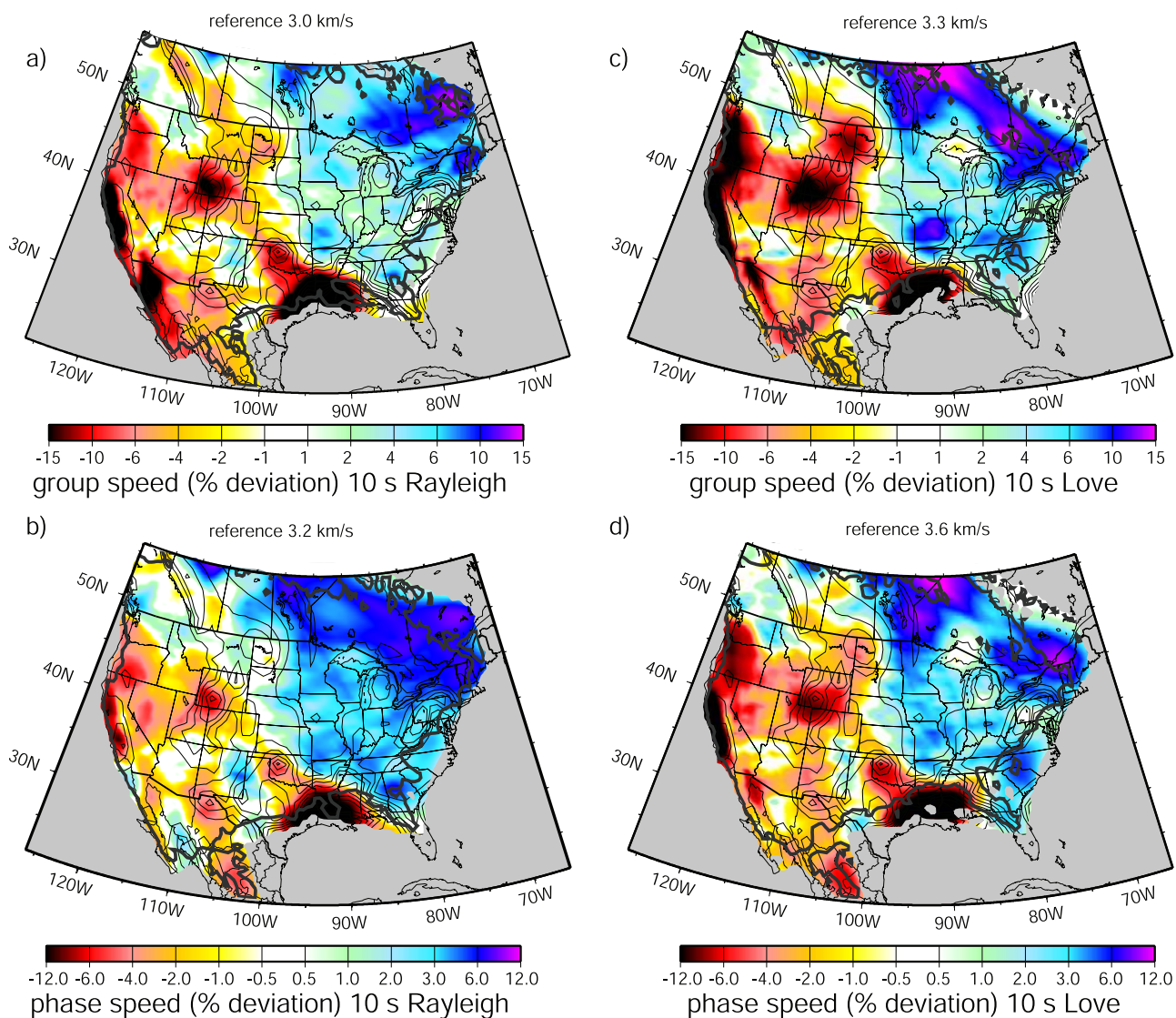


**Figure 12.** Rayleigh and Love wave group and phase speed dispersion maps at 10 s period: (a) Rayleigh group speed, (b) Rayleigh phase speed, (c) Love group speed, and (d) Love phase speed. The thick grey contour outlines the region with better than 200 km resolution and areas with resolution worse than 1000 km are clipped to grey. Many sedimentary features labeled in Figure 18 are visible and 1-km contours of the sediment model of *Laske and Masters* [1997] are plotted with thin black lines for reference. Note the differences in reference speeds and color scale ranges.

the tendency of the inversion to stay at the input model are determined subjectively to supply acceptable fit to the data, while retaining the coherence of large-scale structures and controlling the tendency of streaks and stripes to contaminate the maps. The smoothing or correlation length parameter,  $\sigma$ , is chosen to be 125 km at periods below 25 s and 150 km at longer periods. As with any tomographic inversion, the resulting maps are not unique but the features that we discuss below are common to any reasonable choice of the damping and smoothness parameters.

[38] Discussion of the tomographic maps is guided by the vertical  $V_s$  sensitivity kernels shown in Figure 16. At a given period, phase velocity measurements tend to sense deeper structures than group velocity measurements and Rayleigh waves sense deeper than Love waves. Thus at any

period the Rayleigh wave phase velocities will have the deepest sensitivity and the Love wave group velocities will be most sensitive to shallow structures.

[39] Figures 12 and 13 show Rayleigh and Love wave group and phase speed maps at 10 and 20 s period, respectively. Sedimentary thickness contours are over-plotted in Figure 12 and will be discussed further in the next section. The 10 s maps are all similar to one another, with much lower speeds in the western than the eastern US. The similarity of the maps is expected because these wave types are all predominantly sensitive to crustal structures, notably the existence of sediments. Thus the principal features on these maps are slow anomalies correlated with sedimentary basins, as discussed later. The 20 s maps are also similar to one another, with the exception of the Rayleigh phase

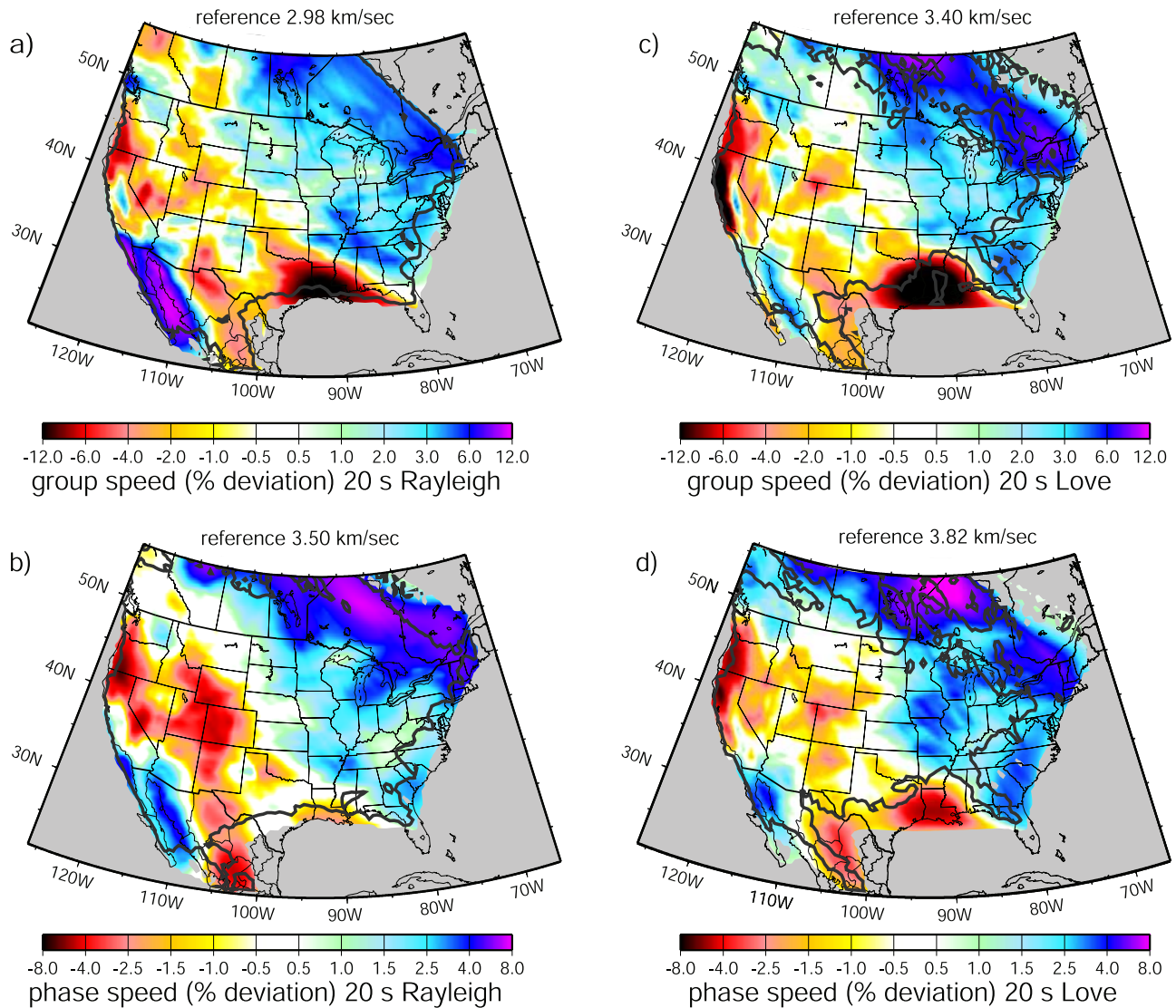


**Figure 13.** Same as Figure 12, but for 20 s period and sedimentary contours are suppressed.

velocity map. The 20 s Rayleigh group velocity and Love wave group and phase velocity maps are more similar to the 10 s maps than the 20 s phase velocity map. This is because, like the 10 s results, these maps are mostly sensitive to the wave speeds within the crust. This similarity between these maps lends credibility to the tomographic results at short periods.

[40] As Figure 16b shows, the 20 s Rayleigh wave phase velocity map has a substantial sensitivity to the mantle and is better correlated with intermediate period maps. Examples of results at intermediate periods are shown in Figure 14, which presents a comparison between the 25 s Rayleigh wave phase speed and the 40 s Rayleigh wave group speed maps. Figure 16c also shows that these two wave types have similar vertical sensitivity kernels, both waves being predominantly sensitive to shear velocities in the uppermost mantle. The measurements, however, are entirely different. We view the similarity between these maps, therefore, as a qualitative confirmation of the procedure at intermediate periods.

[41] The longest period map presented here is the 60 s Rayleigh wave phase speed map shown in Figure 15a. This map possesses considerable sensitivity to the upper mantle to a depth of about 150 km. It is compared to the map for the same wave type computed from the 3-D model of *Shapiro and Ritzwoller [2002]* shown in Figure 15b. At large scales, the maps are similar both in the distribution and absolute value of velocity. Considering all points of 15 with resolution better than 1000 km, the 60 s phase speed map derived from ambient noise is about 2% faster than the results of *Shapiro and Ritzwoller [2002]*. Omitting points near the coast where resolution is lower, this difference decreases to less than 1% faster. A more damped version of the ambient noise map agrees even better with the model prediction.

[42] The fit of individual dispersion measurements to the tomographic maps reveals more about the quality of the data. The first type of information is the variance reduction relative to a homogeneous model, which here is taken to be the average of the measurements at each wave type and

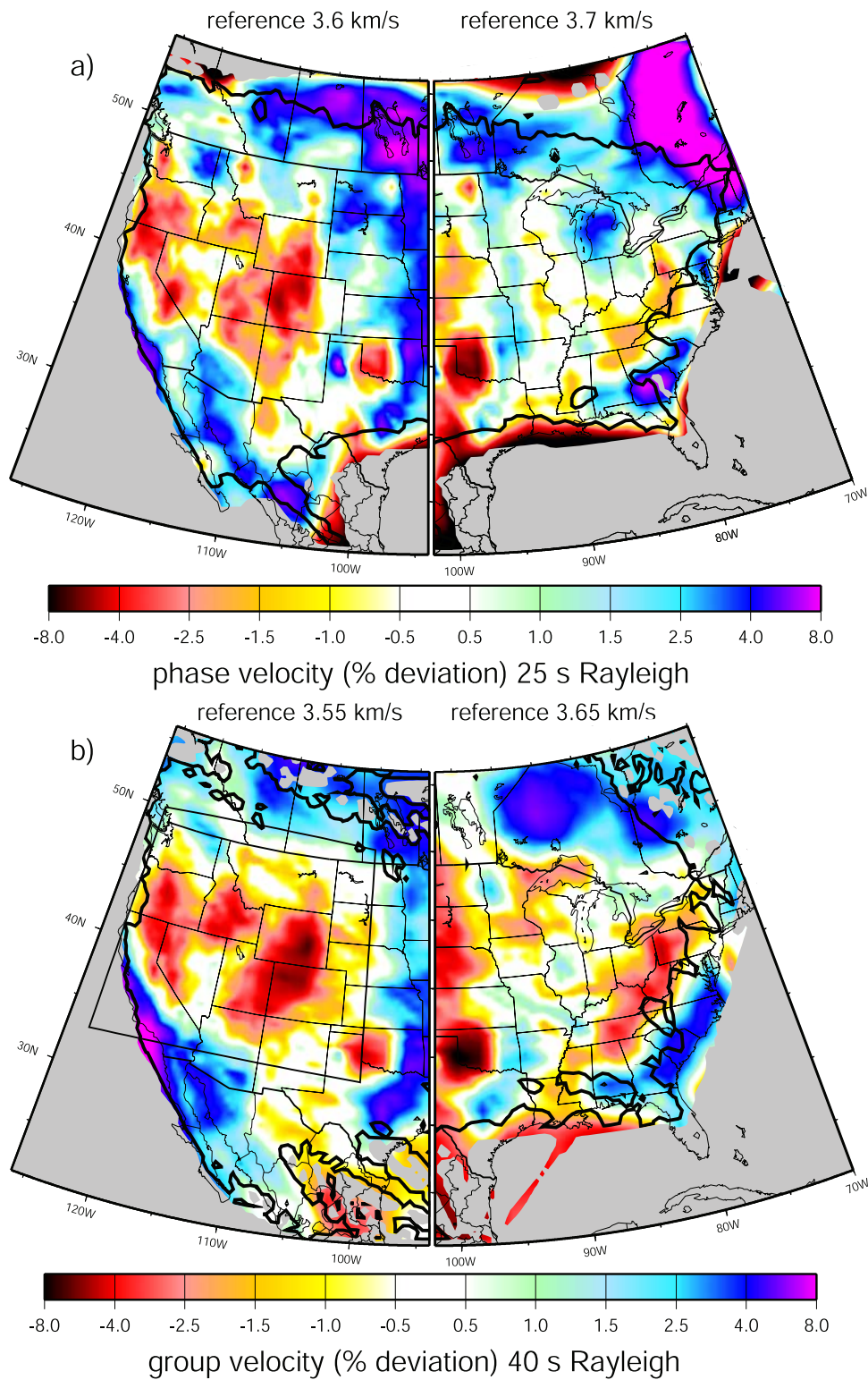


**Figure 14.** (a) The 25 s period Rayleigh wave phase speed map. (b) The 40 s Rayleigh wave group speed map. Grey contours indicate a resolution of 200 km and resolution less than 1000 km is colored grey. Different reference wave speeds are used in each half of the map and are indicated in the figure. The box in Figure 14b corresponds to the region blown up in Figure 19.

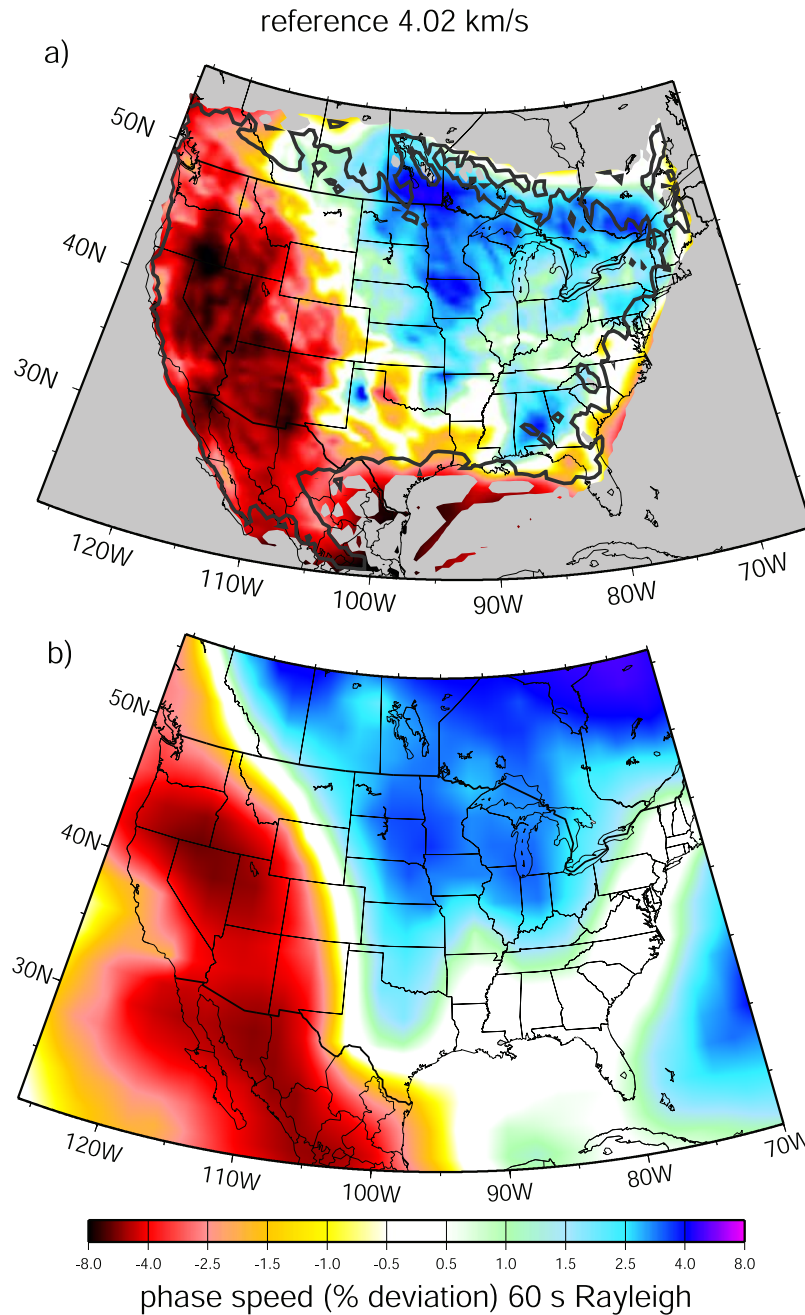


**Figure 15.** (a) The Rayleigh wave phase speed map at 60 s period. The grey contour outlines the 200 km resolution and continental areas with indeterminate velocity are clipped to white. (b) The prediction from a 3-D global model [Shapiro and Ritzwoller, 2002] is shown for comparison.

period. Figure 17a shows the variance reduction for the Rayleigh and Love wave group and phase speed maps from 10 to 90 s period. (Rayleigh wave maps above 70 s period and Love wave maps above 25 s period are created in order to extend these statistics to the longer periods.) The largest variance reductions are for the Rayleigh wave phase velocity measurements, which are above 90% for the entire period range. Below 20 s period, a similar variance reduction is achieved by the Rayleigh wave group speed maps. Love wave variance reduction is mostly lower. Love wave results above about 25 s period are of little meaning because

the number of measurements is so low. For all wave types, the mean path length is about the same (around 1800 km) for all periods. The variance reduction reflects the RMS residual level after tomography, which is plotted both in time and velocity in Figures 17b and 17c. Rayleigh wave RMS phase traveltime residuals are between 2 and 3 s across the whole band, and traveltime residuals for the other wave types are mostly between 6 and 10 s. In particular, Rayleigh wave group traveltimes residuals are 2–3 times larger than the anomalies for Rayleigh phase, consistent

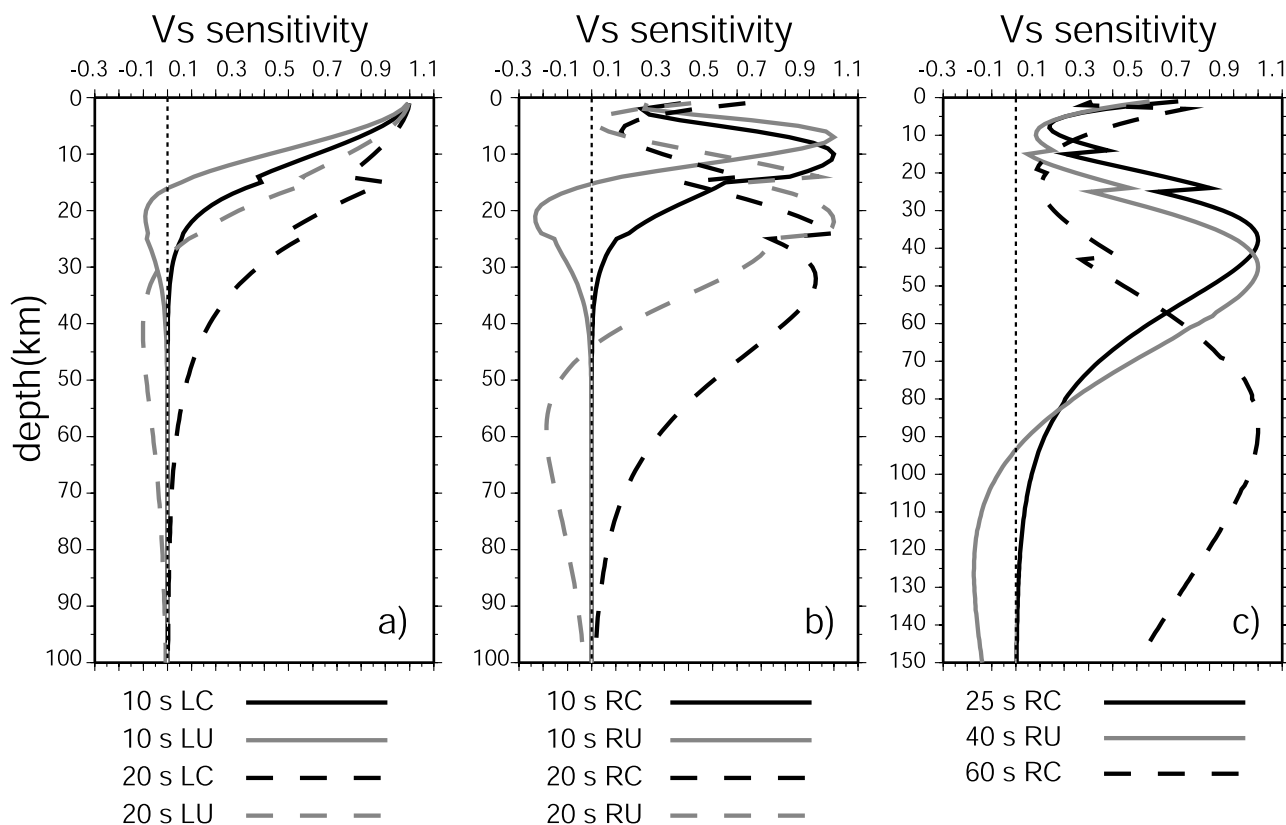


**Figure 16.** Sensitivity kernels for all dispersion maps shown here. Sensitivities for 10 and 20 s period Love waves are shown in Figure 16a, 10 and 20 s period Rayleigh waves are in Figure 16b and longer periods in Figure 16c. The kernels have been normalized to have the same maximum amplitude and the labeling is as follows: RC - Rayleigh phase, RU - Rayleigh group, LC - Love phase, LU - Love group. Kernels are computed for PREM but with the ocean replaced by consolidated sediments.

with the standard deviation of the phase velocity measurement being about half that for group velocity.

## 7. Discussion

[43] Detailed interpretation of surface wave dispersion maps is difficult because their sensitivity kernels are extended in depth and the group velocity kernels they actually change sign. We present a qualitative discussion of Figures 12–15 here, but a more rigorous interpretation must await a 3-D inversion for versus structures in the crust and uppermost mantle, which is beyond the scope of this paper. Many of the features of the maps in Figures 12–15 are not surprising, as they represent structures on a larger spatial scale similar to those revealed by the earlier work of *Shapiro et al.* [2005], *Lin et al.* [2007], and *Moschetti et al.* [2007] in the western US. The details of the maps and how they vary with period, particularly at longer periods and in the eastern US, are entirely new, however.

[44] Overall, the most prominent anomaly on all maps is the continental-scale east-west dichotomy between the tectonically active western US and the cratonic eastern US. This dichotomy is observed at all periods, so it expresses both crustal and mantle structures, although its contribution tends to grow with increasing period, at least in a relative sense. In terms of smaller scale regional structures, lateral crustal velocity anomalies that manifest themselves in

surface wave dispersion maps are largely compositional in origin, whereas the mantle anomalies are probably predominantly thermal, although volatile content may also contribute to low velocity anomalies in both the crust and mantle. The most significant shallow crustal lateral velocity anomalies are due to velocity differences between the sedimentary basins and surrounding crystalline rocks, which are more significant than velocity variations within the crystalline crust. Large-scale anomalies in the uppermost mantle correspond to variations in lithospheric structure and thickness, predominantly reflecting differences between the thin tectonic lithosphere of the western US and the thicker cratonic lithosphere of the eastern and central US. Regional scale anomalies reflect variations in the thermal state of the uppermost mantle and crustal thickness.

[45] Below 20 s period (i.e., Figures 12 and 13), the dispersion maps dominantly reflect low velocity anomalies caused by sedimentary basins. The sediment model of *Laske and Masters* [1997] is shown in Figure 18 for comparison, with several principal structural units identified. Isopach contours are superimposed in Figure 12 with a 1 km interval for reference. The 10 s period maps reveal low velocity anomalies associated with sediments in the Great Valley (CV) of central California as well as the Salton Trough/Imperial Valley of southern California extending down into the Gulf of California (GC). Low velocity anomalies are also coincident with the Anadarko (AB) basin in Texas/

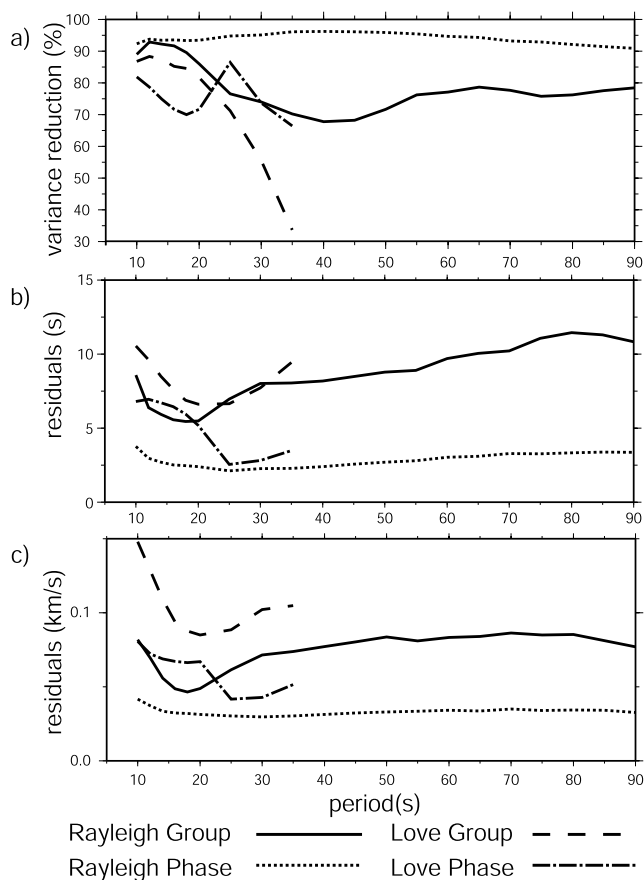


**Figure 17.** (a) Rayleigh and Love wave group and phase speed variance reduction as a function of period, computed relative to the mean measurement for each wave type and period. (b) The RMS final traveltime residuals in s. (c) Final RMS velocity residuals.

Oklahoma and the Permian Basin (PB) in west Texas. The deep sediments in the Gulf of Mexico (GOM) produce the largest low velocity features. Other basins such as the Wyoming-Utah-Idaho thrust belt (TB) extending north to the Williston basin (WB) also are apparent. This feature is seen best on the Love wave group speed map (Figure 12c) which has the shallowest sensitivity (see Figure 16a). Rayleigh wave phase speed on the other hand has deeper sensitivity and the Williston basin is only vaguely seen as a relative low velocity feature in Figure 12b. The Appalachian Basin (ApB) also appears as a relative slow anomaly in all maps, although it is less pronounced due to the generally higher wave speeds and older (hence faster) sediments in the eastern US. The Michigan Basin (MB) is not observed, probably because of the lower resolution in the central US than in west where station coverage is better.

[46] Low wave speeds observed in the 10 s maps for the Basin and Range (BR) and Pacific Northwest (PNW) are interesting considering the lack of deep sedimentary basins. These anomalies, therefore, are probably due to thermal or compositional anomalies within the crystalline crust rather than in the sediment overburden.

[47] Many of the features of the 10 s maps in Figure 12 are also seen in the 20 s maps of Figure 13. The range of depth sensitivities for the 20 s dispersion maps is broad

(Figure 16), however, and the 20 s Rayleigh wave phase speed map (Figure 13b) is more like longer period maps. In addition, the shallower and older basins are not observed and the Sierra Nevada (SN) high velocity anomaly emerges more clearly at 20 s than at 10 s period. High speed anomalies are observed in the Gulf of California, in contrast to the 10 s maps, due to thin oceanic crust.

[48] At intermediate periods (25–40 s), waves are primarily sensitive to depths between 25 and 70 km; namely, the deep crust (in places), crustal thickness, and the uppermost mantle. The Rayleigh wave 25 s phase speed map and the 40 s group speed map have maximum sensitivities at about 50 km depth and similar kernels, as Figure 17 illustrates. Thick crust tends to appear as slow velocity anomalies and thin crust as fast anomalies on the maps. The anomalies on the maps in Figure 14 are similar to one another, with a few exceptions. The low velocity anomalies through the Rocky Mountain Region (RM, Colorado, Wyoming, eastern Utah, southern Idaho) and the Appalachian Mountains (ApM, northern Alabama to western Pennsylvania) are probably the most prominent low velocity features and they reflect thicker crust than average. To focus on this further, the box drawn in the western panel of Figure 14b is shown in greater detail in Figure 19. Over-plotted in this figure is the depth to Moho model of *Seber et al.* [1997] with a 2.5 km contour interval. In general, areas with thicker crust in Nevada, Utah, Idaho, Wyoming, and Colorado have slower wave speeds, as expected. The bone-shaped high velocity anomaly of eastern Nevada corresponds to thinner crust beneath the Great Basin. East of Colorado, however, crustal velocities are higher due to the east-west tectonic dichotomy of the US and the lithosphere thickens beneath cratonic North America, which partially compensates for the low velocities that result from the thick crust. For this reason, the low velocities beneath the Rocky Mountain region do not extend into the central US. Nevertheless, the low velocities of the Colorado Plateau probably also reflect elevated crustal temperatures in addition to thicker crust. High velocity anomalies along the coasts, in southern Arizona, and northwestern Mexico reflect thinner crust in these regions.

[49] Not all low velocity anomalies at intermediate periods have their origin in thicker crust. In the Pacific Northwest (PNW) states of northern California, Oregon, and Washington, slow anomalies are probably caused by a warm, volatilized mantle wedge overlying the subducting Juan de Fuca and Gorda plates. These low velocities are not seen south of the Mendocino triple junction where the subducting slab is no longer present in the shallow mantle. Perhaps surprisingly, the effect of the Anadarko Basin (AB) in western Oklahoma persists to these periods. Figure 16c illustrates that even at intermediate periods very shallow structures will have a contribution to surface wave speeds.

[50] Some features differ between the 25 s group speed and the 40 s phase speed maps, however. We note two. First, the 40 s phase speed map has low velocities extending east into Nebraska and South Dakota, whereas these features are more subdued on the 25 s group speed map. Second, the 25 s group speed map has a high velocity anomaly in Michigan which is largely missing on the 40 s phase speed map, although Michigan does appear as a relatively fast feature

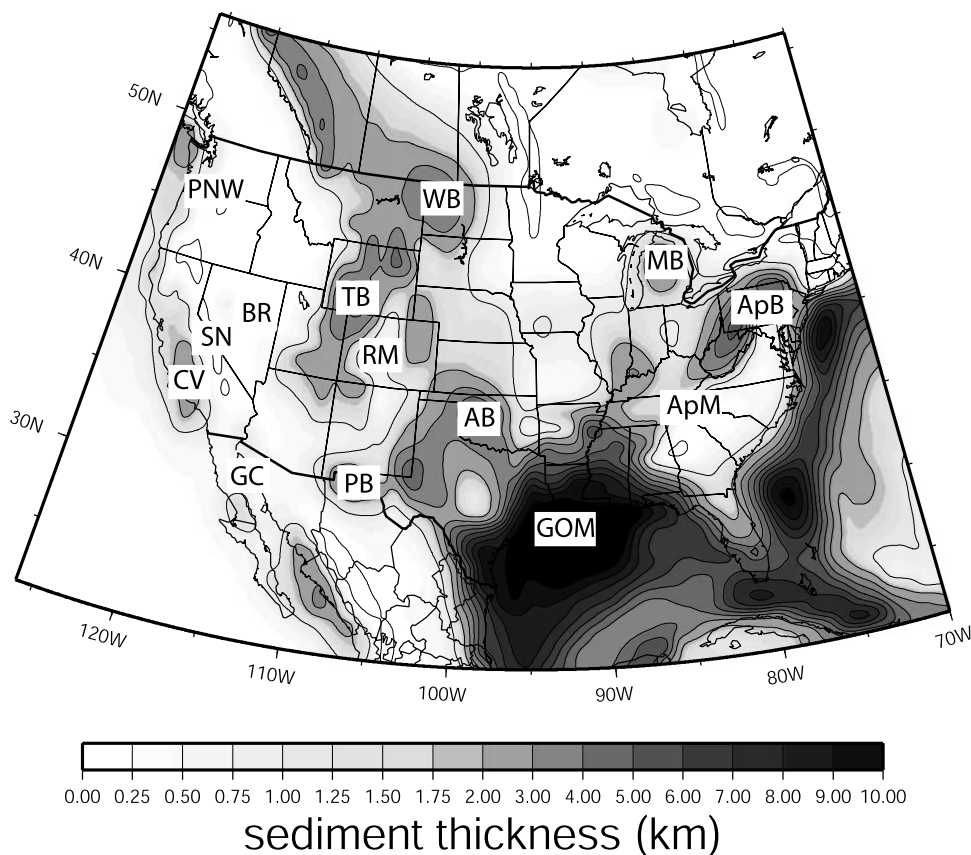


**Figure 18.** Sediment thickness model of *Laske and Masters* [1997] with several prominent basins and geographical features labeled: ‘CV’ - Central Valley in California, ‘SN’ - Sierra Nevada, ‘AB’ - Anadarko Basin, ‘PB’ - Permian Basin, ‘GOM’ - Gulf of Mexico, ‘TB’ - Wyoming-Utah-Idaho thrust belt, ‘WB’ - Williston Basin, ‘ApB’ - Appalachian Basin, ‘MB’ - Michigan Basin, ‘BR’ - Basin and Range, ‘RM’ - Rocky Mountain Region, ‘ApM’ - Appalachian Mountains, ‘PNW’ - Pacific Northwest, ‘GC’ - Gulf of California.

in this map. These discrepancies are small, and overall the maps agree quite well.

[51] Moving to deeper mantle sensitivity, Figure 15a shows the phase speed map at 60 s period. This wave is most sensitive to depths from 50 to 150 km and reveals features of mantle structure and lithospheric thickness, in contrast to the shallower sensitivity of maps in Figure 14. The cold, thick lithosphere beneath the cratonic core of the continent appears clearly as a fast anomaly in the central and eastern US, while the thinner lithosphere in the western United States appears as low velocities over a large area. The transition between the tectonic and cratonic lithosphere is similar in both maps, but the ambient noise map reveals more of a stair-step latitudinal structure rather than the more continuous variation with latitude found in the 3-D model prediction. The lowest velocities of the map are in the high lava plains of southeast Oregon and northwest Nevada, which is believed to be the location of the first surface expression of the plume that currently underlies Yellowstone. Yellowstone itself is below the resolution of the maps presented in this study. However, a low velocity anomaly does appear in the maps derived from ambient noise tomography based on the Transportable Array component of EarthScope/USArray [Moschetti *et al.*, 2007; Lin *et al.*,

2007]. Very low velocities are also associated with the Sierra Madre Occidental in western Mexico, which is a Cenozoic volcanic arc.

## 8. Conclusions

[52] We computed cross-correlations of long time sequences of ambient seismic noise to produce Rayleigh and Love wave empirical Green functions between pairs of stations across North America. This is the largest spatial scale at which ambient noise tomography has been applied, to date. Cross-correlations were computed using up to two years of ambient noise data recorded from March of 2003 to February of 2005 at  $\sim 200$  permanent and temporary stations across the US, southern Canada, and northern Mexico. The period range of this study is from about 5 to 100 s. We show that at all periods and most azimuths across the US, coherent Rayleigh wave signals exist in ambient noise. Thus ambient noise in this frequency band across the US is sufficiently isotropically distributed in azimuth to yield largely unbiased dispersion measurements.

[53] Rayleigh and Love wave group and phase speed curves were obtained for every inter-station path, and uncertainty estimates (standard deviations) were determined

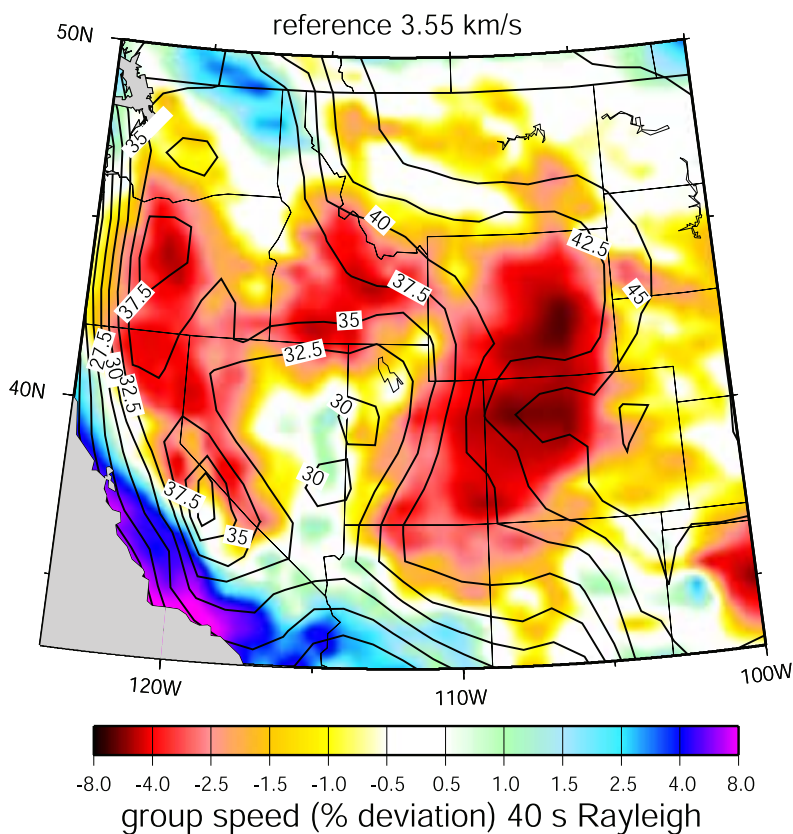


**Figure 19.** Rayleigh wave group speed dispersion map at 40 s period for the region outlined in Figure 14b. The Cornell US Moho depth model [Seber *et al.*, 1997] is plotted as contours with a 2.5 km contour interval with a maximum thickness (of 47 km) under Colorado. Low velocities generally correspond to thick crust.

from the variability of temporal subsets of the measurements. Phase velocity standard deviations are about half the group velocity standard deviations, on average. These uncertainty estimates and the frequency dependent signal-to-noise ratios were used to identify the robust dispersion curves, with total numbers changing with period and wave type up to a maximum of about 8500. Sufficient numbers of measurements (more than 2000) to perform surface wave tomography were obtained for Love waves between about 8 and 25 s period and for Rayleigh waves between about 8 and 70 s period. A subset of these maps are presented herein. Resolution (defined as twice the standard deviation of a 2-D Gaussian function fit to the resolution surface at each point) is estimated to be better than 100 km across much of the US at most periods, but it degrades at the longer periods and degenerates sharply near the edges of the US, particularly near coastlines. This resolution is unprecedented in a study at the spatial scale of this one.

[54] In general, the dispersion maps agree well with each other and with known geological features and, in addition, provide new information about structures in the crust and uppermost mantle beneath much of the US. Inversion to estimate 3-D Vs structure in the crust and uppermost mantle and to constrain crustal anisotropy are natural extensions of this work.

[55] **Acknowledgments.** All of the data used in this research were downloaded either from the IRIS Data Management Center or the Canadian National Data Center (CNDC). This research was supported by a contract from the US Department of Energy, DE-FC52-2005NA26607, and two grants from the US National Science Foundation, EAR-0450082 and EAR-0408228 (GEON project support for Bensen).

## References

- Alsina, D., R. L. Woodward, and R. K. Snieder (1996), Shear wave velocity structure in North America from large-scale waveform inversions of surface waves, *J. Geophys. Res.*, *101*(B7), 15,969–15,986.
- Barmin, M. P., M. H. Ritzwoller, and A. L. Levshin (2001), A fast and reliable method for surface wave tomography, *Pure Appl. Geophys.*, *158*(8), 1351–1375.
- Bensen, G. D., M. H. Ritzwoller, M. P. Barmin, A. L. Levshin, F. Lin, M. P. Moschetti, N. M. Shapiro, and Y. Yang (2007), Processing seismic ambient noise data to obtain reliable broad-band surface wave dispersion measurements, *Geophys. J. Int.*, (169), 1239–1260.
- Butler, R., et al. (2004), The global seismographic network surpasses its design goal, *EOS Trans.*, *85*(23), 225–229.
- Campillo, M., and A. Paul (2003), Long-range correlations in the diffuse seismic coda, *Science*, *299*(5606), 547–549.
- Cho, K. H., R. B. Herrmann, C. J. Ammon, and K. Lee (2007), Imaging the upper crust of the Korean Peninsula by surface-wave tomography, *Bull. Seismol. Soc. Am.*, *97*(1B), 198–207.
- Derode, A., E. Larose, M. Campillo, and M. Fink (2003), How to estimate the Green's function of a heterogeneous medium between two passive sensors? Application to acoustic waves, *Appl. Phys. Lett.*, *83*(15), 3054–3056.
- Ekström, G., J. Tromp, and E. W. F. Larson (1997), Measurements and global models of surface wave propagation, *J. Geophys. Res.*, *102*(B4), 8137–8157.
- Gerstoft, P., K. Sabra, P. Roux, W. Kuperman, and M. Fehler (2006), Green's functions extraction and surface-wave tomography from microseisms in southern California, *Geophysics*, *71*(4), 23–31.

- Godey, S., R. Snieder, A. Villaseñor, and H. M. Benz (2003), Surface wave tomography of North America and the Caribbean using global and regional broad-band networks: Phase velocity maps and limitations of ray theory, *Geophys. J. Int.*, *152*(3), 620–632.
- Larose, E., A. Derode, M. Campillo, and M. Fink (2004), Imaging from one-bit correlations of wideband diffuse wave fields, *J. Appl. Phys.*, *95*(12), 8393–8399.
- Larose, E., A. Derode, D. Clorennec, L. Margerin, and M. Campillo (2005), Passive retrieval of Rayleigh waves in disordered elastic media, *Phys. Rev. E*, *72*(4), 046,607(8), doi:10.1103/PhysRevE.72.046607.
- Laske, G., and G. Masters (1997), A global digital map of sediment thickness, *EOS Trans. AGU*, *78*, 483.
- Levshin, A. L., V. F. Pisarenko, and G. A. Pogrebinsky (1972), On a frequency-time analysis of oscillations, *Ann. Geophys.*, *28*(2), 211–218.
- Lin, F., M. H. Ritzwoller, J. Townend, M. Savage, and S. Bannister (2007), Ambient noise Rayleigh wave tomography of New Zealand, *Geophys. J. Int.*, *170*(2), doi:10.1111/j.1365-246X.2007.03414.x.
- Lin, F., M. P. Moschetti, and M. H. Ritzwoller (2008), Surface wave tomography of the western United States from ambient seismic noise: Rayleigh and Love wave phase velocity maps, *Geophys. J. Int.*, doi:10.1111/j.1365-246X.2008.03720.x.
- Lobkis, O. I., and R. L. Weaver (2001), On the emergence of the Green's function in the correlations of a diffuse field, *J. Acoust. Soc. Am.*, *110*(6), 3011–3017.
- Moschetti, M. P., M. H. Ritzwoller, and N. M. Shapiro (2007), Surface wave tomography of the western United States from ambient seismic noise: Rayleigh wave group velocity maps, *Geochem. Geophys. Geosyst.*, *8*, Q08010, doi:10.1029/2007GC001655.
- Ritzwoller, M. H., and A. L. Levshin (1998), Eurasian surface wave tomography - Group velocities, *J. Geophys. Res.*, *103*(B3), 4839–4878.
- Ritzwoller, M. H., N. M. Shapiro, M. P. Barmin, and A. L. Levshin (2002), Global surface wave diffraction tomography, *J. Geophys. Res.*, *107*(B12), 2335, doi:10.1029/2002JB001777.
- Sabra, K. G., P. Gerstoft, P. Roux, W. Kuperman, and M. C. Fehler (2005), Surface wave tomography from microseisms in Southern California, *Geophys. Res. Lett.*, *32*, L14311, doi:10.1029/2005GL023155.
- Seber, D., M. Vallvé, E. Sandvol, D. Steer, and M. Barazangi (1997), Middle East tectonics: Applications of Geographic Information Systems (GIS), *GSA Today*, *7*(2), 1–6.
- Shapiro, N. M., and M. Campillo (2004), Emergence of broadband Rayleigh waves from correlations of the ambient seismic noise, *Geophys. Res. Lett.*, *31*, L07614, doi:10.1029/2004GL019491.
- Shapiro, N. M., and M. H. Ritzwoller (2002), Monte-Carlo inversion for a global shear-velocity model of the crust and upper mantle, *Geophys. J. Int.*, *151*(1), 88–105.
- Shapiro, N. M., M. Campillo, L. Stehly, and M. H. Ritzwoller (2005), High-resolution surface-wave tomography from ambient seismic noise, *Science*, *307*(5715), 1615–1618.
- Snieder, R. K. (2004), Extracting the Green's function from the correlation of coda waves: A derivation based on stationary phase, *Phys. Rev. E*, *69*(4), 046,610(8).
- Spetzler, J., J. Trampert, and R. K. Snieder (2002), The effect of scattering in surface wave tomography, *Geophys. J. Int.*, *149*(3), 755–767.
- Stehly, L., M. Campillo, and N. M. Shapiro (2006), A study of the seismic noise from its long-range correlation properties, *J. Geophys. Res.*, *111*(B10), B10306, doi:10.1029/2005JB004237.
- Stehly, L., M. Campillo, and N. M. Shapiro (2007), Traveltime measurements from noise correlation: Stability and detection of instrumental time-shifts, *Geophys. J. Int.*, *171*(1), doi:10.1111/j.1365-246X.2007.03492.x.
- Tanimoto, T., and K. P. Sheldrake (2002), Three-dimensional S-wave velocity structure in Southern California, *Geophys. Res. Lett.*, *29*(8), 1223, doi:10.1029/2001GL013486.
- Trampert, J., and J. H. Woodhouse (1996), High resolution global phase velocity distributions, *Geophys. Res. Lett.*, *23*(1), 21–24.
- van der Lee, S., and G. Nolet (1997), Upper mantle S velocity structure of North America, *J. Geophys. Res.*, *102*(B10), 22,815–22,838.
- Villaseñor, A., Y. Yang, M. H. Ritzwoller, and J. Gallart (2007), Ambient noise surface wave tomography of the Iberian Peninsula: Implications for shallow seismic structure, *Geophys. Res. Lett.*, *34*, L11304, doi:10.1029/2007GL030164.
- Wapenaar, K. (2004), Retrieving the elastodynamic Green's function of an arbitrary inhomogeneous medium by cross correlation, *Phys. Rev. Lett.*, *93*(25), 254,301(4), doi:10.1103/PhysRevLett.93.254301.
- Weaver, R. L., and O. I. Lobkis (2001), Ultrasonics without a source: Thermal fluctuation correlations at MHz frequencies, *Phys. Rev. Lett.*, *87*(13), 134,301(4), doi:10.1103/PhysRevLett.87.134301.
- Yang, Y., and M. H. Ritzwoller (2008), The characteristics of ambient seismic noise as a source for surface wave tomography, *Geochem. Geophys. Geosyst.*, *9*, Q02008, doi:10.1029/2007GC001814.
- Yang, Y., M. H. Ritzwoller, A. L. Levshin, and N. M. Shapiro (2007), Ambient noise Rayleigh wave tomography across Europe, *Geophys. J. Int.*, *168*(1), 259–274.
- Yao, H., R. D. van der Hilst, and M. V. de Hoop (2006), Surface-wave array tomography in SE Tibet from ambient seismic noise and two-station analysis-I. Phase velocity maps, *Geophys. J. Int.*, *166*(2), 732–744.
- Yoshizawa, K., and B. L. N. Kennett (2002), Determination of the influence zone for surface wave paths, *Geophys. J. Int.*, *149*(2), 440–453.

G. D. Bensen and M. H. Ritzwoller, Center for Imaging the Earth's Interior, Department of Physics, University of Colorado at Boulder, Campus Box 390, Boulder, CO 80309-0390, USA. (gbensen@colorado.edu)

N. M. Shapiro, Laboratoire de Sismologie, CNRS, IGP, Paris, France.